Forest carbon densities and uncertainties from Lidar, QuickBird, and field measurements in California

Patrick Gonzalez [a],[*], Gregory P. Asner [b], John J. Battles [a],[c], Michael A. Lefsky [d],
Kristen M. Waring [a],[1], Michael Palace [e],[f]

[a] Center for Forestry, University of California, Berkeley, CA 94720-3114, USA
[b] Department of Global Ecology, Carnegie Institution, Stanford, CA 94305-4101, USA
[c] Department of Environmental Science, Policy, and Management, University of California, Berkeley, CA 94720-3114, USA
[d] Department of Forest, Rangeland, and Watershed Stewardship, Colorado State University, Fort Collins, CO 80523-1472, USA
[e] Complex Systems Research Center, University of New Hampshire, Durham, NH 03824-3525, USA
[f] Environmental Change Institute, Oxford University, Oxford OX1 3QY, UK

ARTICLE INFO

ABSTRACT

Greenhouse gas inventories and emissions reduction programs require robust methods to quantify carbon sequestration in forests. We compare forest carbon estimates from Light Detection and Ranging (Lidar) data and QuickBird high-resolution satellite images, calibrated and validated by field measurements of individual trees. We conducted the tests at two sites in California: (1) 59 km^2 of secondary and old-growth coast redwood (_Sequoia sempervirens_) forest (Garcia–Mailliard area) and (2) 58 km^2 of old-growth Sierra Nevada forest (North Yuba area). Regression of aboveground live tree carbon density, calculated from field measurements, against Lidar height metrics and against QuickBird-derived tree crown diameter generated equations of carbon density as a function of the remote sensing parameters. Employing Monte Carlo methods, we quantified uncertainties of forest carbon estimates from uncertainties in field measurements, remote sensing accuracy, biomass regression equations, and spatial autocorrelation. Validation of QuickBird crown diameters against field measurements of the same trees showed significant correlation ($r = 0.82$, $P < 0.05$). Comparison of stand-level Lidar height metrics with field-derived Lorey's mean height showed significant correlation (Garcia–Mailliard $r = 0.94$, $P < 0.0001$; North Yuba $R = 0.89$, $P < 0.0001$). Field measurements of five aboveground carbon pools (live trees, dead trees, shrubs, coarse woody debris, and litter) yielded aboveground carbon densities (mean $\pm$ standard error without Monte Carlo) as high as 320 ± 35 Mg ha^{-1} (old-growth coast redwood) and 510 ± 120 Mg ha^{-1} (red fir [_Abies magnifica_] forest), as great or greater than tropical rainforest. Lidar and QuickBird detected aboveground carbon in live trees, 70–97% of the total. Large sample sizes in the Monte Carlo analyses of remote sensing data generated low estimates of uncertainty. Lidar showed lower uncertainty and higher accuracy than QuickBird, due to high correlation of biomass to height and undercounting of trees by the crown detection algorithm. Lidar achieved uncertainties of <1%, providing estimates of aboveground live tree carbon density (mean $\pm$ 95% confidence interval with Monte Carlo) of 82 ± 0.7 Mg ha^{-1} in Garcia–Mailliard and 140 ± 0.9 Mg ha^{-1} in North Yuba. The method that we tested, combining field measurements, Lidar, and Monte Carlo, can produce robust wall-to-wall spatial data on forest carbon.

© 2010 Elsevier Inc. All rights reserved.

1. Introduction

A growing forest naturally removes greenhouse gases from the atmosphere and reduces the magnitude of global climate change. Global vegetation and soils removed carbon from the atmosphere at a rate (mean $\pm$ 66% confidence interval) of 4.7 ± 1.2 Gt y^{-1} in 2008, compared to fossil fuel emissions of 8.7 ± 0.5 Gt y^{-1} and deforestation

emissions of 1.2 ± 0.7 Gt y^{-1} (Intergovernmental Panel on Climate Change [IPCC], 2007; Le Quéré et al., 2009). Parties to the United Nations Framework Convention on Climate Change (UNFCCC) and jurisdictions such as the State of California, USA, conduct national and sub-national greenhouse gas inventories. Furthermore, the UNFCCC and other institutions have established greenhouse gas emissions reduction programs with credits for forest conservation, afforestation, and reforestation. Greenhouse gas inventories and emissions reduction programs require scientifically robust methods to quantify forest carbon storage over time across extensive landscapes.

Monitoring forest carbon in forests with high spatial variation of tree density and species composition poses major challenges (Fahey

---

* Corresponding author.
  E-mail address: pgonzalez@cal.berkeley.edu (P. Gonzalez).
[1] Present address: School of Forestry, Northern Arizona University, Flagstaff, AZ 86011-5018, USA.

et al., 2009). The financial cost of forest inventory can render it infeasible as the sole method for estimating the forest carbon of extensive areas. In addition, forest inventory programs that are funded sufficiently for large-scale forest carbon monitoring, such as the Forest Inventory and Analysis (FIA) program of the United States Department of Agriculture (USDA) Forest Service, use large administrative areas as units of analysis (Woodbury et al., 2007), masking local variability.

Remote sensing, calibrated by field measurements, addresses these challenges. Methods commonly calculate forest carbon as the product of surface areas of land cover types, classified by satellite systems with moderate spectral or spatial resolutions, e.g. Landsat and MODIS, and mass of carbon per unit area (carbon density), derived from field measurements of trees and allometric equations, summed over all land cover types (Achard et al., 2004; Blackard et al., 2008; DeFries et al., 2007; Potter et al., 2008; Saatchi et al., 2007). The number of land cover types that satellites with moderate spectral or spatial resolutions can accurately discriminate, generally five to twenty classes (Bartholomé & Belward, 2005; Loveland et al., 2000; Sánchez-Azofeifa et al., 2009), limits the possible carbon density of each pixel to a few discrete values.

In contrast to satellites with moderate spectral or spatial resolutions, high-resolution Lidar and high-resolution satellites such as QuickBird, IKONOS, WorldView, and GeoEye sense physical dimensions of trees to which aboveground biomass directly correlates. With these systems, forest carbon content equals the product of the area and the carbon density of each pixel, where carbon density is calculated by applying allometric equations to field measurements of individual trees and correlated to canopy height metrics estimated by Lidar or tree crown diameter estimated by high-resolution satellite data. This method generates raster coverage of the spatial distribution of forest carbon density with continuous values.

Field research has demonstrated the accuracy of Lidar estimates of canopy height (Andersen et al., 2006; Magnussen & Boudewyn, 1998; Næsset, 1997; 2009) and high correlation of Lidar height metrics to field-measured aboveground biomass (Boudreau et al., 2008; Drake et al., 2002; Hurtt et al., 2004; Hyde et al., 2006; Lefsky et al., 1999; 2005; Næsset & Gobakken, 2008) and forest carbon density (Balzter et al., 2007; Patenaude et al., 2004). Financial and expertise requirements of Lidar methods have prevented their widespread adoption for forest carbon monitoring in tropical countries, although it has been tested in the Brazilian Amazon (Asner, 2009). Lidar has produced more accurate estimates of forest biomass than Landsat (Lefsky et al., 2001), high spectral resolution sensors (Lefsky et al., 2001), and synthetic aperture radar (Sexton et al., 2009). Direct comparison of Lidar to high-resolution satellites for forest carbon monitoring remains an area for further investigation because these two systems are potential tools for national

greenhouse gas inventories (Bickel et al., 2006) and reducing emissions from deforestation and degradation (REDD) programs (DeFries et al., 2007).

Research on high-resolution optical images from QuickBird and IKONOS has tested algorithms to detect crown diameter and other tree characteristics in a wide range of forest biomes (Asner et al., 2002; Clark et al., 2004; Palace et al., 2008; Thenkabail et al., 2004; Wulder et al., 2004). High-resolution satellites can detect individual tree crowns but the accurate monitoring of forest carbon has not been fully demonstrated.

The choice of remote sensing system will influence the levels of uncertainty in the estimates of forest carbon. To quantify uncertainty of forest carbon estimates, the IPCC (2006) recommends Monte Carlo analysis, which reduces uncertainty compared to simple combination of confidence intervals of equation variables (Mandel, 1984). Research has applied Monte Carlo analysis to forest carbon at regional (Chambers et al., 2007) and national (Monni et al., 2007) scales, although not all forest carbon studies quantify uncertainty.

We have sought to advance the application of remote sensing to forest carbon monitoring through research that provides new information on the capabilities of Lidar and high-resolution satellites, on carbon densities of high-biomass forests, and on uncertainties of forest carbon estimates. Our research objectives are: (1) to directly compare forest carbon estimates from Lidar data and QuickBird high-resolution satellite images, calibrated and validated by field measurements of individual trees, (2) to estimate forest carbon densities in two high-biomass forests in California, and (3) to quantify, with Monte Carlo analysis, uncertainties in forest carbon estimates from uncertainties in field measurements, remote sensing accuracy, biomass regression equations, and spatial autocorrelation.

2. Methods

2.1. Garcia–Mailliard research area

The Garcia–Mailliard research area (Fig. 1) consists of two separate units between 38.89° and 38.93° N and 123.32° and 123.55° W: (1) 58 km² eastern half of the private Garcia River forest and (2) 1 km² Mailliard Redwoods State Natural Reserve (SNR). Located in the North Coast Range of California, the area consists of low ridges and shallow valleys. Garcia River forest is secondary coast redwood forest with post-harvest stands approximately 20–80 years old. The California Climate Action Registry has registered a carbon project in Garcia River forest. Mailliard Redwoods SNR, established in 1945, consists of old-growth coast redwood forest, although not as tall as old-growth coast redwood forests further north in California with forest carbon
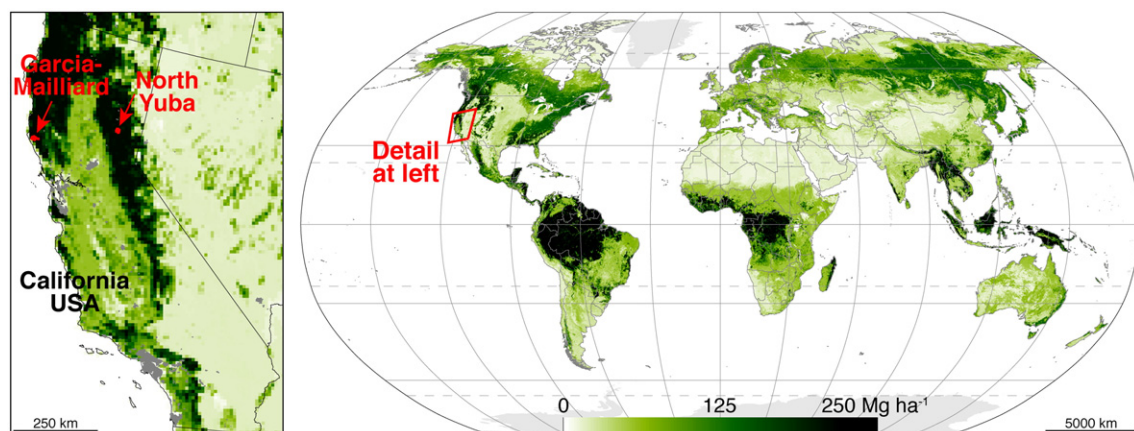

Fig. 1. Location of research areas. Background shows aboveground vegetation carbon density (Matthews et al., 2000) derived from AVHRR remote sensing (Loveland et al., 2000) and field measurements (Olson et al., 1983), analyzed at 10 km spatial resolution.

densities of 1600–2900 t ha^{-1}, the highest in the world (Busing & Fujimori, 2005).

2.2. North Yuba research area

The North Yuba research area covers 58 km^2 between 39.60° and 39.70° N and 120.76° and 120.86° W in the Tahoe National Forest, California, USA (Fig. 1). Protected since 1891 as a part of the former Sierra Forest Reserve, eight watersheds in the northern part of the Yuba River Old Forest Emphasis Area (USDA Forest Service, 2004b) form the research area. Mountain ridges and deep creek valleys create steep topography. Three forest types cover the area: (1) mixed oak and Douglas-fir forest at lower elevations, (2) mid-elevation mixed conifer forest, and (3) red fir forest at high elevation. Shrub lands and scree slopes occur at high elevations.

2.3. Field measurements

Field measurements furnished data to calibrate Lidar and Quick-Bird estimates of aboveground biomass, assess the accuracy of Lidar canopy height metrics, directly validate QuickBird-derived tree crown diameter, and characterize forest types. To compare results to regional forest inventories of the USDA Forest Service (Christensen et al., 2008), we used a modified FIA design (USDA Forest Service, 2004a).

We estimated the approximate number of field plots (n_{plots}) needed (Husch et al., 2003):

$$n_{plots} = t^2 CV^2 \left(\frac{1}{E}\right)^2 \qquad (1)$$

where t is the value of Student's t distribution for n_{plots} at $P = 0.05$, CV is the coefficient of variation (ratio [%] of the standard deviation and mean of the forest carbon density), and E is the estimated allowable error (% of the mean). For CV, we used FIA percent sampling error values (USDA Forest Service, 2009) for redwood forest in the North Coast region (Garcia–Mailliard) and mixed conifer forest in the Sacramento Valley region (North Yuba). For $E = 20\%$, a common starting point (Husch et al., 2003), $n_{plots} = 38$ plots (Garcia–Mailliard) and 26 plots (North Yuba). We established 40 plots in Garcia–Mailliard and 39 plots in North Yuba. This is greater than the 30 required for a statistical sample (von Storch & Zwiers, 1999) and near the 40 to 50 needed to calibrate Lidar (Zhao et al., 2009). The cost of field work constrained the number of plots.

In Garcia–Mailliard, we established a stratified random sample of 40 permanent forest plots, stratified by management history and tree size (Fig. 2). In Garcia, we placed seven plots at random in each of the four California Department of Forestry and Fire Protection (2003) Landsat and field-determined classes of diameter at breast height (*dbh*; at height [*h*] = 1.37 m): $dbh \leq 2.5$ cm, $2.5 < dbh \leq 15$ cm, 15 cm $< dbh \leq 28$,
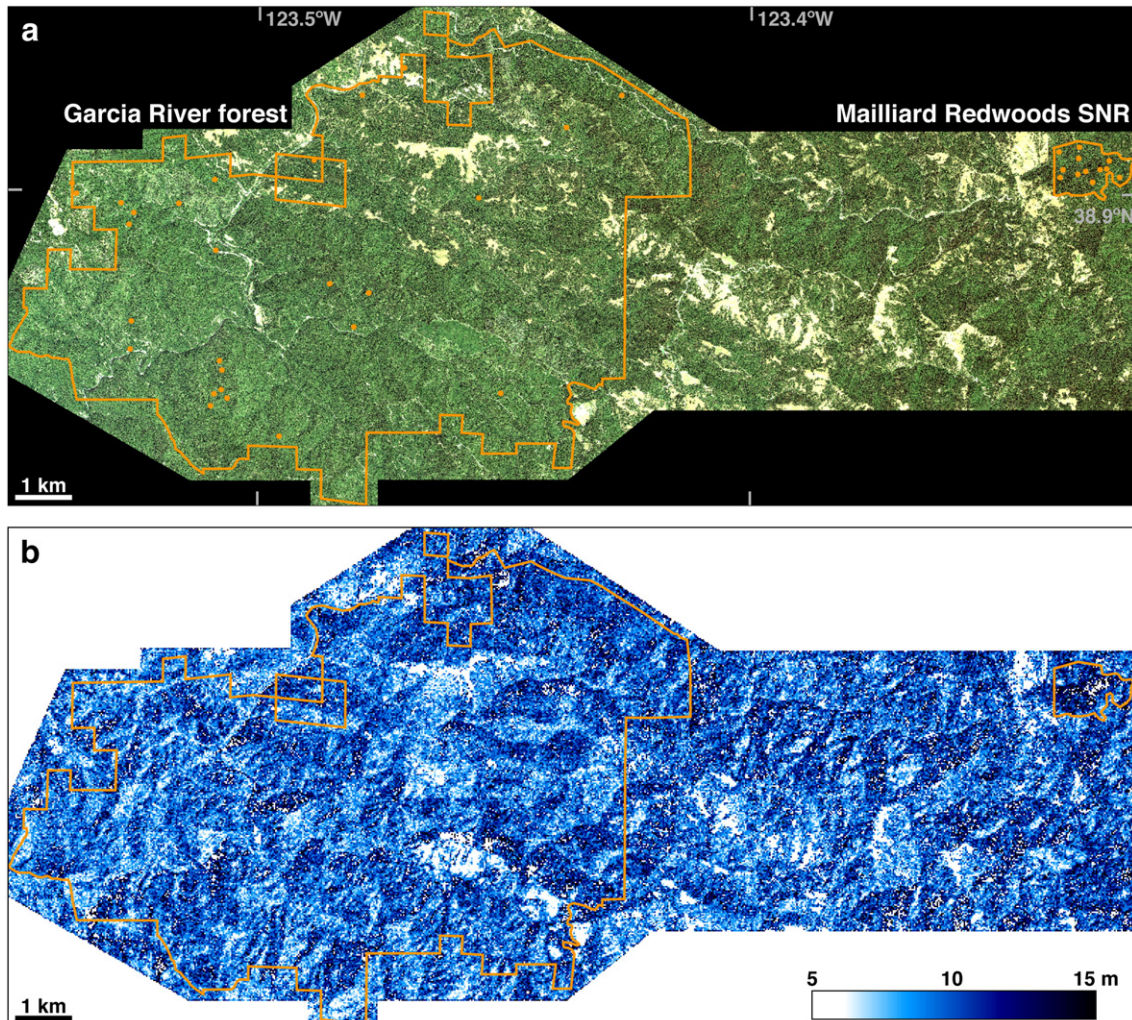

Fig. 2. Garcia–Mailliard research area. (a) QuickBird panchromatic sharpened multi-spectral image, research area perimeters, and field plot locations. (b) QuickBird crown diameter.

$28 < dbh \leq 61$. In Mailliard, where forest structure was homogeneous, we placed 12 plots at random. In North Yuba, we established a systematic sample of 36 modified FIA plots on a 1.25 km geographic grid originating at 39.70° N, 120.86° W (Fig. 3). We retained three additional plots established at the beginning of field work off the grid in the most abundant forest type, for a total sample size of 39 plots. A Trimble

Pathfinder ProXT differential GPS receiver recorded plot center coordinates with an accuracy of <1 m.

Each modified FIA plot is a cluster of four circular 17.95 m radius annular plots with one central 0.1 ha annular plot, three satellite 0.1 ha annular plots, four 7.32 m subplots, and one 2.77 m radius microplot (Fig. 4). Each modified FIA plot also contains three 17.95 m long transects from the cluster center, with the first transect positioned at a random azimuth and the others at 60° and 120° from the first transect. In North Yuba, the 36 plots on the grid include all four annular plots. The three non-grid plots have the central annular plot, but no satellite annular plots. In Garcia–Mailliard, all 40 plots contain four annular plots.

Following FIA methods, we have only used data from the central annular plots for the forest carbon estimates. In the central annular plots, we tagged (at $h = 1.5$ m) and measured every tree of $dbh \geq 19.5$ cm, the minimum diameter for dominant and co-dominant canopy conifers in the region (van Mantgem & Stephenson, 2005). For hardwood species in Garcia–Mailliard central annular plots, we measured trees of $dbh \geq 29.5$ cm, which we observed was the typical minimum diameter for dominant canopy hardwoods. We recorded species and measured dbh (at $h = 1.37$ m). For all of the trees of $dbh \geq 19.5$ cm in one quadrant selected at random, we also measured height, live crown vertical length, and crown horizontal diameter in the four cardinal directions. In the central subplots, we located each tree of $dbh \geq 12.5$ cm (Garcia–Mailliard) or $dbh \geq 5$ cm (North Yuba) (thresholds from USDA Forest Service (2004a)) and $dbh < 19.5$ cm, recorded the species, and measured dbh. For the first ten trees of this size starting from the north, we also measured total height, live crown length, and crown width in the four cardinal directions. We measured a non-random sample of additional trees of this size to ensure representation of all tree species.

To directly validate QuickBird tree crown diameters, we randomly selected 74 trees (Garcia–Mailliard) and 26 trees (North Yuba) of $dbh \geq 19.5$ cm, recorded the direction and range of the trees from the plot center, and measured the eight ordinal crown radii.

To assess whether Lidar height metrics at the stand level accurately reflected canopy heights in the field, we calculated Lorey's mean height (h_L, m), for each central annular plot:

$$h_L = \overset{\text{all trees}}{\sum} gh \bigg/ \overset{\text{all trees}}{\sum} g \qquad (2)$$

where g is the basal area (m^2) and h is the height (m) of each live tree of $dbh \geq 19.5$ cm. For those trees with unmeasured heights, we derived 17 species-specific equations of h as a function of dbh (Appendix A), selecting equations with the lowest Akaike's Information Criterion (AIC; Burnham & Anderson, 1998). Measured and calculated heights showed significant correlation to dbh (Garcia, $r = 0.81$, $P < 0.0001$, $n = 262$; Maillard, $r = 0.93$, $P < 0.0001$, $n = 102$; North Yuba, $r = 0.89$, $P < 0.0001$, $n = 412$).

We measured additional parameters to quantify carbon in small trees, coarse woody debris, and shrubs. In the microplots, we located each tree of $dbh < 12.5$ cm (Garcia–Mailliard) or $dbh < 5$ cm (North Yuba) and recorded species and dbh to the nearest centimeter. We tallied trees of $h < 1.37$ m into two classes ($h < 0.5$ m, $0.5 \leq h < 1.37$ m). Along each transect, we measured coarse woody debris by locating each piece of wood of diameter >19.5 cm and length >1 m and recorded decay class, measured length of intersection, diameters at intersection and small and large ends, and total length. For shrubs, we located patches of $h \geq 1$ m and intersection length ≥ 1 m, recorded species, and measured length and height at the beginning, middle, and end. In North Yuba, we measured fire fuels along the inner 12.62 m length of the transect, following the protocol of Brown (1974).

2.4. Lidar

From September 14 to 17, 2005, we collected Lidar data using an Optech ALTM 2050 system on an airplane flying at an altitude of
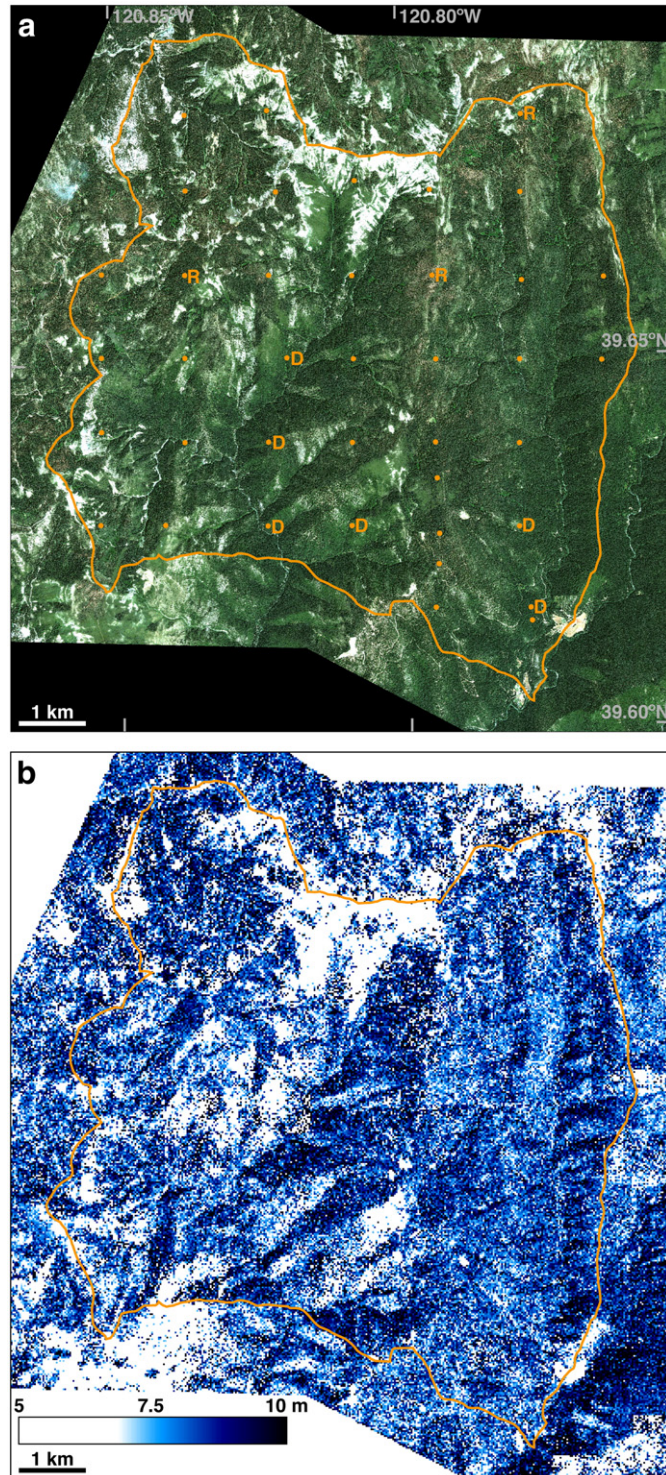
Fig. 3. North Yuba research area. (a) QuickBird panchromatic sharpened multi-spectral image, research area perimeter, and field plot locations (D = Oak–Douglas-fir, R = red fir, all others = mid-elevation mixed conifer). (b) QuickBird crown diameter.

Central annular plot (17.95 m radius)

Central subplot (7.32 m radius)

Microplot (2.07 m radius,

3.66 m and 90° from center)

Satellite annular plot (17.95 m radius)

Satellite subplot (7.32 m radius)

Shrub and CWD transect (17.95 m length)
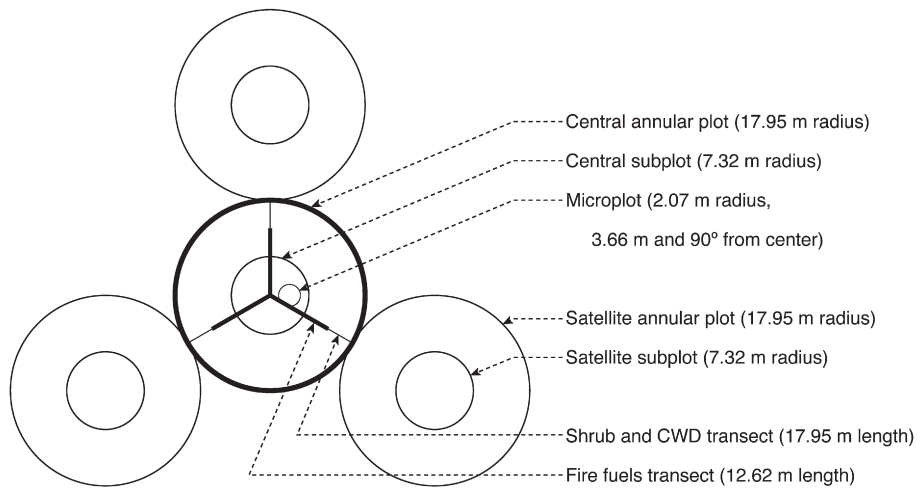
Fire fuels transect (12.62 m length)

Fig. 4. Field plot, modified from FIA (USDA Forest Service, 2004a) design.

800 m and average velocity of 260 km h^{-1}. The ALTM 2050 acquired up to three returns per pulse at a pulse frequency of 50 kHz, point density of 1 shot m^{-2}, scan frequency of 38 Hz, and a maximum scan angle of 15°, creating a swath width of 580 m. Optech, Inc. rates the root mean square error (RMSE) precision of individual point locations surveyed by the ALTM 2050 as ±15 cm vertical and ±50 cm horizontal. In steep areas, point locations may be less precise due to distortion of the returned Gaussian envelope.

Lidar gives the elevation of each scanned point, either on the tree canopy or the ground surface. Application of a progressive morphological filter (Zhang et al., 2003) to Lidar data removed non-ground points through stepwise detection of sharp changes in elevation that indicated the presence of individual trees. This automated iterative method progressive removed changes in elevation that occurred at scales smaller than the scale of each filter in a series. We produced a digital elevation model (DEM) of the ground surface at a spatial resolution of 2 m (Garcia–Mailliard) or 5 m (North Yuba).

We estimated canopy height as the difference between the Lidar-detected elevation of a point and the derived DEM elevation under that point. Because the 1 shot m^{-2} spatial density is sparse, it is unlikely that the shots fell on the exact tops of trees. This prevented calibration of Lidar data to individual trees. Therefore, we generated canopy height metrics at the stand level, at a spatial resolution of 25 m, the width of a square pixel that would fit entirely inside a 17.95 m radius circular field plot. We later resampled 25 m Lidar-derived biomass data to a spatial resolution of 31.8 m, the width of a square pixel with the same surface area as a 17.95 m radius circular field plot. Using all Lidar points within each 25 m pixel, we calculated mean height, quadratic mean height, maximum height, and height percentiles at 10% intervals. The numerical values of these height metrics are not intended to exactly match the values of the corresponding heights of the actual canopy. Instead, the Lidar canopy height metrics comprise variables for the derivation of regression equations of aboveground biomass as a function of Lidar data.

Because the sparse density of the Lidar points prevented validation of Lidar data against measurements of individual trees, we assessed Lidar accuracy through linear regression (Garcia–Mailliard) or stepwise multiple regression (North Yuba) of Lidar canopy height metrics to h_L of the 17.95 radius circle of each central annular plot, a method developed by Næsset (1997). Because Lidar laser pulses sample the forest canopy with a probability of reflection proportional to the area of the exposed tree crowns, and because tree crown area is proportional to tree basal area, the correlation of Lidar height metrics to h_L of field plots indicates whether Lidar produces accurate indices of the actual height of the forest canopy.

2.5. QuickBird

The QuickBird satellite acquired cloud-free images of the Garcia–Mailliard research area at 12:16 PM Pacific Daylight Time (PDT) on August 7, 2005 (Fig. 2a) and the North Yuba research area at 12:10 PM PDT on August 2, 2005 (Fig. 3a) from a sun-synchronous orbital altitude of 450 km. QuickBird captured images composed of one band of panchromatic data at 0.6 m spatial resolution and four bands of multi-spectral data at 2.4 m spatial resolution, with each band at 11 bit data depth. Digital Globe, Inc. provided orthorectified QuickBird data with a horizontal accuracy (RMSE) of 6.2 m.

To classify forest and non-forest areas, we first calculated the normalized difference vegetation index (NDVI; Tucker, 1979). We conducted a K-means unsupervised classification on the QuickBird multi-spectral bands and NDVI. Forest areas showed a mean digital number (DN) value ≥ 102 (out of 2048).

For forest areas, we used an automated crown detection method to locate tree crowns and determine crown diameters (Palace et al., 2008). The algorithm outlines tree crowns by iterative local maximum filtering of the panchromatic band and transect determination of local minima. Because the top of the crown is typically the most brightly illuminated part of a tree, the algorithm iteratively sets crown centers at local brightness maxima. Next, an automated sub-routine runs transects from each brightness maximum outward in 360 ordinal directions (one per degree) and terminates each transect when a change in pixel-to-pixel brightness exceeds a user-defined threshold. This threshold is often image-dependent and cannot be readily generalized for all image types, scene brightness levels, and sun-ground-sensor geometries. After tracing the edge of each tree crown, the algorithm calculates the mean diameter of each crown.

Because of the computational demand of the automated crown detection method, we divided the research areas into 1 km × 1 km tiles, ran the algorithm, and recompiled the tiles into full images. Prior to executing the code on the entire image, we conducted multiple runs on the entire Mailliard Redwoods SNR and on one North Yuba image tile to test the sensitivity of the crown detection method to NDVI forest mask values and transect termination thresholds. Based on these tests and on extensive manual interpretation of the imagery, we set the NDVI forest mask to 0.45 and termination threshold to 2 for Garcia–Mailliard and NDVI forest mask to 0.6 and termination threshold to zero for North Yuba. Comparison of the crown detection test results with the panchromatic images showed that crown detections with centroid pixel values of DN < 350 were often false, so we removed those detections.

The crown delineation algorithm produced vector files with each tree crown as a separate feature. We quantified accuracy by directly

validating QuickBird-estimated crown diameter against field-measured crown diameter. We conducted linear regression of QuickBird-estimated crown radius (dependent variable) against field-measured crown radius (independent variable) for 100 trees measured in the field and precisely located in the QuickBird images. We used the longest field-measured crown radius of eight ordinal radii because the crown detection algorithm estimates tree diameters based on the longest ordinal transect.

2.6. Carbon density from field measurements

From field measurements, we calculated the mass per unit area (carbon density) in each plot cluster of aboveground live biomass (trees and shrubs), aboveground dead matter (trees and coarse woody debris), and litter. For Garcia–Mailliard, we calculated the carbon density of aboveground live biomass and dead matter carbon pools, but not litter.

We used species-specific allometric equations (Busing & Fujimori, 2005; Jenkins et al., 2003, 2004; Means, 2005; Pillsbury & Kirkley, 1984; Ter-Mikaelian & Korzukhin, 1997; Wensel & Krumland, 1983; Westman, 1987) to estimate tree biomass from measurements of diameter and height (Appendix A). We selected allometric equations derived in forest types, seral classes, and tree sizes most similar to our data. When necessary, we used wood specific gravity (Jenkins et al., 2004) to convert tree wood volume to mass.

The allometric equations for California black oak (Quercus kelloggii), canyon live oak (Quercus chrysolepis), Douglas-fir (Pseudotsuga menziesii), Pacific madrone (Arbutus menziesii), and western white pine (Pinus monticola) required height in addition to dbh. We used height equations from Larsen and Hann (1987) for oaks and madrone and from Hanus et al. (1999) for western white pine. With field measurements of 37 trees, we verified that the oak and madrone equation accurately calculated height. Field measurements of six trees showed that the western white pine equation overestimated height by 45%. Therefore, we reduced calculated heights of western white pine by 45% before applying biomass allometric equations.

For three species, we derived regression equations of h as a function of dbh measured at $h = 1.37$ m (Table 1a–c). The sample for these equations included all measured trees in Garcia and Mailliard combined, whereas the height equations for the Lidar accuracy assessment were developed separately for Garcia and Mailliard (Appendix A).

Total aboveground tree biomass density ($B_{\text{live trees}}$, Mg ha^{-1}) equals:

$$B_{\text{live trees}} = \sum^{\text{all trees}} \left(\frac{b_{\text{tree}}}{A_{\text{plot}}}\right)\left(\frac{1\,\text{Mg}}{10^3\,\text{kg}}\right) \tag{3}$$

where b_{tree} is the aboveground biomass (kg) of a tree calculated from the allometric equations, and A_{plot} is the area (ha) of the annular plot, subplot, or microplot where the tree was counted. $B_{\text{live trees}}$ includes all live trees of all diameters.

To develop an equation of shrub biomass in North Yuba as a function of shrub area, we selected ten greenleaf manzanita (Arctostaphylos patula) and huckleberry oak (Quercus vaccinifolia) shrubs that represented the range of growth forms. For each stem, we measured canopy area, height, and occupied volume, then cut and weighed the wet mass of all aboveground biomass. We also collected and dried three biomass samples to determine moisture content. Among different predictors of dry mass, canopy area yielded the biomass regression equation with the most significant probability (Table 1d). Shrub aboveground biomass density (B_{shrubs}, Mg ha^{-1}) for each annular plot equals:

$$B_{\text{shrubs}} = \left(\frac{1}{A_{\text{annular}}}\right)\left(-0.8811 + 1.23\frac{\sum^{\text{all shrubs}} l_{\text{intersection}}}{l_{\text{transect}}}\left(\frac{1\,\text{m}}{10^2\,\text{cm}}\right)A_{\text{annular}}\right)\left(\frac{1\,\text{Mg}}{10^3\,\text{kg}}\right) \tag{4}$$

where A_{annular} is the annular plot area of 0.1012 ha, $l_{\text{intersection}}$ is the length (cm) of the intersection of the piece with the transect, and l_{transect} is the transect length of 17.95 m.

Because most dead trees did not have many attached branches, we calculated mass of dead trees as 70% of the equivalent biomass of a live tree. The mass per unit area of dead trees ($M_{\text{dead trees}}$, Mg ha^{-1}) is:

$$M_{\text{dead trees}} = \sum^{\text{all dead trees}} \left(\frac{0.7\ b_{\text{tree}}}{A_{\text{plot}}}\right)\left(\frac{1\,\text{Mg}}{10^3\,\text{kg}}\right). \tag{5}$$

Table 1
Allometric equations derived from field measurements and remote sensing.

	r^2	R^2	P	AIC	RMSE	SE	n
Tree height							
(a) *Lithocarpus densiflorus:* $h = (67.5499\ dbh)/(97.7877 + dbh)$	0.42		<0.0001				105
(b) *Pseudotsuga menziesii:* $h = (88.01\ dbh)/(108.03 + dbh)$	0.89		<0.001				91
(c) *Sequoia sempervirens:* $h = (110.371\ dbh)/(148.152 + dbh)$	0.80		<0.001				106
Shrub biomass							
(d) $b_{\text{shrub}} = -0.8811 + 1.23 A_{\text{canopy}}$	0.91		0.026				10
Lidar biomass							
(e) Garcia–Mailliard: $B_{\text{live trees}} = 6.1660695\ h_q + 0.5045322 h_q^2$		0.86	0.009		98		40
(f) North Yuba: $B_{\text{live trees}} = 27.488705 h_q - 46.41089\ h_{10} + 48.094323 h_{20} - 45.54945 h_{30}$ $+ 61.757518 h_{40} - 36.13169 h_{50} - 12.5304$		0.80	0.0001		123		39
QuickBird biomass							
(g) Garcia: $\ln(b_{\text{tree}} * 10^6) = 8.573 d_{\text{crown}}^{0.2078}$	0.55			7.8		2.2	261
(h) Mailliard: $\ln(b_{\text{tree}} * 10^6) = 8.82 d_{\text{crown}}^{0.2217}$	0.59			3.1		2.8	102
(i) North Yuba: $\ln(b_{\text{tree}} * 10^6) = 8.7719 d_{\text{crown}}^{0.2492}$	0.73			−0.8		3.0	331

Variables: A_{canopy} = area of shrub canopy (m^2), AIC = Akaike's Information Criterion, b_{shrub} = aboveground biomass of a shrub (kg shrub^{-1}), b_{tree} = aboveground biomass of a tree (Mg tree^{-1}), $B_{\text{live trees}}$ = aboveground live tree biomass density (Mg ha^{-1}), d_{crown} = crown diameter (m), dbh = diameter at breast height (at height = 1.37 m) (cm), h = height (m), h_j = height at the jth percentile of points in the Lidar pixel (m), h_q = quadratic mean height of Lidar canopy points in a pixel (m), n = sample size, P = probability, r^2 = coefficient of determination from bivariate regression, R^2 = coefficient of determination from multivariate regression, RMSE = root mean square error (Mg ha^{-1}), SE = Standard error of the mean (Mg tree^{-1}).

For coarse woody debris (CWD), we calculated the mass of each measured piece (m_{piece}, kg; Harmon & Sexton, 1996):

$$m_{piece} = \left(\frac{\rho_{CWD} l_{piece}}{3}\right)\left(\frac{1\,kg}{10^3\,g}\right)$$
$$\times \left[\pi\left(\left(\frac{d_{large}}{2}\right)^2 + \left(\frac{d_{small}}{2}\right)^2\right) + \sqrt{\pi\left(\left(\frac{d_{large}}{2}\right)^2 + \left(\frac{d_{small}}{2}\right)^2\right)}\right] \quad (6)$$

where ρ_{CWD} is the wood density (0.50 g cm^{-3} for weathered wood, 0.32 g cm^{-3} for intermediate decayed wood, 0.17 g cm^{-3} for rotten wood), l_{piece} is the length of the piece (cm), d_{large} is the diameter of the large end (cm), and d_{small} is the diameter of the small end (cm). CWD mass per unit area (M_{CWD}, Mg ha^{-1}) is:

$$M_{CWD} = \sum^{all\,pieces} \left(\frac{\pi}{2l_{intersection}}\right)\left(\frac{10^2\,cm}{m}\right)\left(\frac{m_{piece}}{l_{transect}}\right)\left(\frac{1\,Mg}{10^3\,kg}\right)\left(\frac{10^4\,m^2}{ha}\right). \quad (7)$$

For litter, we used the methods of Brown (1974) to calculate mass per unit area (M_{litter}, Mg ha^{-1}).

Density of aboveground biomass and dead matter ($B_{aboveground}$, Mg ha^{-1}) is:

$$B_{aboveground} = B_{live\,trees} + B_{shrubs} + M_{dead\,trees} + M_{CWD} + M_{litter}. \quad (8)$$

We calculated $B_{aboveground}$ and $B_{live\,trees}$ for each plot and the mean and standard error for each forest type. We converted $B_{aboveground}$ and $B_{live\,trees}$ to carbon units:

$$C_{component} = f_C B_{component} \quad (9)$$

where $C_{component}$ is the carbon density (Mg ha^{-1}) of the aboveground component or live tree pool, f_C is the carbon fraction of biomass (0.47 g carbon [g biomass]$^{-1}$; McGroddy et al., 2004), $B_{component}$ is the aboveground or live tree biomass density (Mg ha^{-1}).

2.7. Carbon densities from Monte Carlo analyses

We used a Monte Carlo approach to quantify the uncertainty in the final estimates of $C_{live\,trees}$, separately for the field measurements, Lidar, and QuickBird. We evaluated the major sources of uncertainty identified in IPCC guidelines (Aalde et al., 2006) and by Wang et al. (2005), including field measurement error, remote sensing accuracy, biomass regression equations, and spatial autocorrelation.

For each analysis, we calculated a mean value of $C_{live\,trees}$ for each sample unit (field plot or pixel), generated 100 (remote sensing) or 1000 (field measurements) realizations of $C_{live\,trees}$ using normally distributed random values of standard error (SE) of individual variables in the equations of $C_{live\,trees}$, and calculated the mean and confidence interval of $C_{live\,trees}$ for the forest parts of each research area.

We analyzed the remote sensing data at two spatial resolutions: 25 m, the width of a square that would fit inside a 17.95 m radius circular field plot, and 31.8 m, the width of a square with the same surface area as a 17.95 m radius circular field plot.

2.7.1. Monte Carlo analyses of field measurement data

In the analyses of field data, we explicitly included the following sources of error: (1) field measurement errors of tree diameter, (2) statistical uncertainty of tree allometric equations, and (3) sampling error of $B_{live\,trees}$ within each research area. We generated 1000 realizations of b_{tree} for each tree, adding error terms for (1) and (2) to the original values of dbh and b_{tree}, respectively:

$$\hat{b}_{tree} = f(dbh + X_{dbh} SE_{dbh}) + X_{allometric} SE_{allometric} \quad (10)$$

where the hat symbol "^" denotes the form of a variable that includes a modeled estimate of error, f(x) denotes function of x, $X_{variable}$ is a random number (different for each variable) from a normal distribution with mean = 0 and standard deviation (SD) = 1, SE_{dbh} is the standard error of dbh, and $SE_{allometric}$ is the standard error of each allometric equation. We estimated SE_{dbh} as the diameter error from repeated measures of a random sample of 169 trees (19 cm < dbh < 148 cm). SE_{dbh} equaled 0.027, expressed as the relative RMSE of the difference between the initial diameter measurement and the repeated measure. For $SE_{allometric}$, we used the SE of regression of each tree allometric equation. In effect, these realizations simulated the potential results of 1000 field campaigns. For each plot, we calculated 1000 realizations of $B_{live\,trees}$ with Eq. (3). We then calculated 1000 realizations of $C_{live\,trees}$ for each plot, adding a term for the sampling error of $B_{live\,trees}$ within each research area to the mean value of $B_{live\,trees}$ for each plot:

$$\hat{C}_{live\,trees}^{plot} = f_C\left(\bar{B}_{live\,trees}^{plot} + X_{live\,trees}^{plot} SE_{live\,trees}^{research\,area}\right) \quad (11)$$

where the overbar symbol "¯" denotes the mean of a variable and $SE_{live\,trees}$ is a function of the sample design of each research area (Woolley et al., 2007). The mean $C_{live\,trees}$ for each research area is:

$$\bar{C}_{live\,trees}^{research\,area} = \left(\frac{1}{n}\right)\sum^{all\,plots}\left(\frac{1}{1000}\right)\left(\sum^{all\,realizations} \hat{C}_{live\,trees}^{plot}\right) \quad (12)$$

where n is the number of plots. The 95% confidence interval (CI) equals:

$$CI = \frac{C_{97.5} - C_{2.5}}{2} \quad (13)$$

where $C_{97.5}$ and $C_{2.5}$ are the 97th and 2.5th percentiles, respectively, of the 1000 realizations of the mean $C_{live\,trees}$ for each research area.

To compare uncertainties of Lidar and QuickBird, we calculated:

$$Uncertainty = \frac{CI}{\bar{C}_{live\,trees}^{research\,area}}. \quad (14)$$

Table 2
Forest characteristics from field measurements. Counts are given for live and dead trees ($dbh \geq 19.5$ cm) tagged and measured in the central annular plots and live and dead trees (all diameters) measured in the satellite annular plots, central and satellite subplots, and microplots. Diameters (mean ± SD) are calculated from central annular plots. Tree densities (mean ± SD) are calculated from central and satellite annular plots.

	Plots		Trees counted		Species richness		Diameter (dbh)	Tree densities ($dbh \geq 19.5$ cm)		Tree densities ($dbh < 19.5$ cm)		Shrub cover (%)	Shrub maximum height (m)
							($dbh \geq 19.5$ cm)						
	Central	Satellite	Central	Other	Tree	Shrub	Live (cm)	Live	Dead	Live	Dead		
	(plots)		(trees)		(species)			(trees ha^{-1})					
Garcia	28	84	1008	1290	10	2	38 ± 15	329 ± 153	8 ± 19	1700 ± 1400	180 ± 500	11	3.5
Mailliard	12	36	390	736	9	1	55 ± 31	333 ± 157	20 ± 23	860 ± 800	160 ± 270	<1	2.1
North Yuba	39	108	1523	1412	11	10	40 ± 21	326 ± 172	60 ± 66	1700 ± 1400	300 ± 400	20	2.8

Table 3
Forest characteristics from remote sensing. For Lidar, forest includes areas where h_{50} > the maximum height of shrubs measured in the field plots (Table 2). For QuickBird, forest includes areas where of d_{crown} > algorithm detection threshold (Garcia–Mailliard 3 m, North Yuba 2.4 m).

	Lidar	Lidar		QuickBird		Lidar	QuickBird			
	Elevation (m)	Forest area				Maximum height (mean ± SD) (m)	Trees delineated (trees)	Tree density		Crown diameter (mean ± SD) (m)
		25 m	31.8 m	25 m	31.8 m			25 m	31.8 m	
		(% of research area)						(trees ha^{-1})		
Garcia	62–679	95	95	97	98	29 ± 5	847 019	150	148	8.3 ± 3.8
Mailliard	317–556	99.8	99.7	92	96	53 ± 9	8776	96	92	9.9 ± 4.1
Garcia–Mailliard	62–679	95	95	97	98	30 ± 6	855 795	149	147	8.3 ± 3.8
North Yuba	1061–2172	72	72	88	91	34 ± 13	421 137	84	80	8.2 ± 2.0

Although we designed the field plot networks in this research primarily to calibrate and validate the remote sensing data, we have calculated mean forest carbon densities and uncertainties at the level of the research area for qualitative comparisons with Lidar and QuickBird.

2.7.2. Monte Carlo analyses of Lidar data

In the analyses of Lidar data, we explicitly included the following sources of error: (1) field measurement biomass uncertainty, calculated above, (2) statistical uncertainty of regression equations of biomass as a function of Lidar height metrics, and (3) spatial autocorrelation of Lidar-derived estimates of biomass density.

To calculate carbon density from Lidar data, we used stepwise multiple regression to develop equations of field measurement-derived aboveground live tree biomass ($B_{live\ trees}$) as a function of Lidar-derived height metrics. Table 1e–f gives the Lidar biomass regression equations with the best fit.

We propagated the uncertainty of field plot biomass estimates through the Lidar biomass regression equations by using the 1000 realizations of $B_{live\ trees}$ for each field plot cluster to generate 1000 realizations of each equation and calculate the RMSE of the median of the 1000 equation realizations. This error propagation integrated the effect of field errors into the Lidar uncertainty estimates. Applying the Lidar biomass regression equations (Table 1e–f) to the Lidar height metrics, we calculated the mean $B_{live\ trees}$ of each 25 m pixel in each research area. We used nearest neighbor resampling on mean $B_{live\ trees}$ at 25 m spatial resolution to generate a separate raster file of mean $B_{live\ trees}$ at 31.8 m spatial resolution.
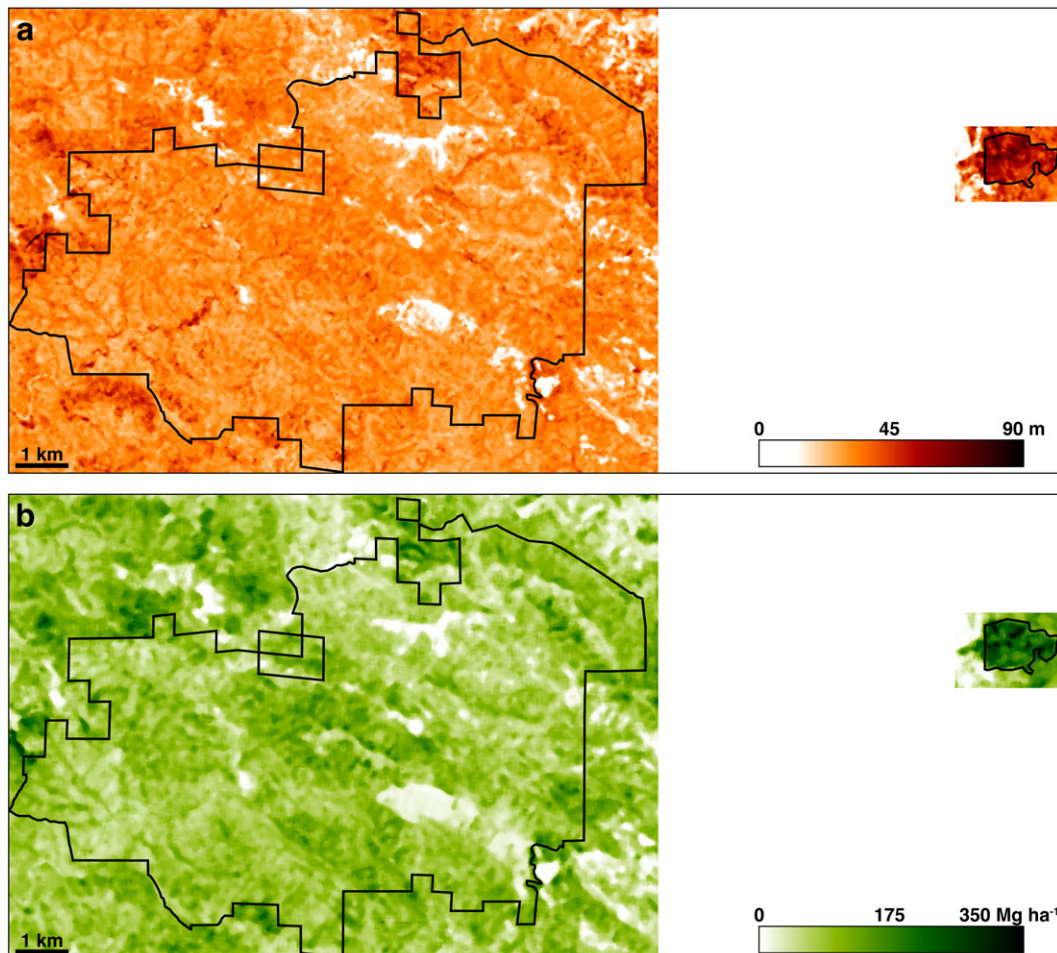

Fig. 5. Garcia–Mailliard research area. (a) Lidar maximum canopy height. (b) Aboveground live tree carbon, from field measurements, Lidar, and Monte Carlo analyses.

For each research area and each spatial resolution, we calculated 100 realizations of $C_{\text{live trees}}$ of each pixel, adding to the mean value of $B_{\text{live trees}}$ a term for the combined field and regression errors and another term for spatial autocorrelation:

$$\hat{C}_{\text{live trees}}^{\text{pixel}} = f_C \left[\bar{B}_{\text{live trees}}^{\text{pixel}} + \left(X_{\text{field + regression}} RMSE_{\text{field + regression}} \right) \right. \qquad (15)$$
$$\left. + \left(X_{\text{autocorrelation}} |I_{\text{local}}| RMSE_{\text{field + regression}} \right) \right]$$

where $RMSE_{\text{field + regression}}$ (Mg ha^{-1}) is the RMSE of the median of the 1000 equation realizations and I_{local} is local Moran's I, an index of spatial autocorrelation that varies from 1 (complete positive correlation) to 0 (no correlation) to −1 (complete negative correlation) (Anselin, 1995), calculated for the mean $B_{\text{live trees}}$ of each pixel at a lag of one pixel. Calculation of the spatial autocorrelation term follows the method of Barrett et al. (2001). A lag of one pixel produces the highest value of I_{local} and, therefore, the highest estimate of uncertainty. We also calculated global Moran's I (I_{global}; Anselin, 1995) for each entire research area.

The mean $C_{\text{live trees}}$ for each research area is:

$$\bar{C}_{\text{live trees}}^{\text{research area}} = \left(\frac{1}{n} \right) \overset{\text{all pixels}}{\sum} \left(\frac{1}{100} \right) \left(\overset{\text{all realizations}}{\sum} \hat{C}_{\text{live trees}}^{\text{pixel}} \right) \qquad (16)$$

where n is the number of pixels in forest areas (height [m] at the 50th percentile of points in the Lidar pixel (h_{50})>maximum height of shrubs measured in the field inventories) of each research area. We then calculated CI (Eq. (13)), and uncertainty (Eq. (14)).

2.7.3. Monte Carlo analyses of QuickBird data

In the analyses of QuickBird data, we explicitly included the following sources of error: (1) crown delineation sensitivity to NDVI forest mask values and transect termination thresholds, (2) crown delineation accuracy based on validation of QuickBird crown estimates against field measurements, (3) statistical uncertainty of regression equations of biomass as a function of crown diameter, and (4) spatial autocorrelation of QuickBird-derived estimates of biomass density.

To calculate carbon density from QuickBird data, we developed allometric equations of aboveground biomass of a tree (b_{tree}, g tree^{-1}) as a function of crown diameter from field measurements of trees in central annular plots, separately for Garcia, Mailliard, and North Yuba (Table 1g–i). We estimated model parameters with likelihood methods (Canham & Uriarte, 2006; Edwards, 1992), quantifying the strength of alternative functional forms with AIC. In general, biomass increases with height and crown diameter, although we were uncertain of the exact form of the best equation and therefore compared various monotonically increasing models and saturating models. We fit parameters using a simulated annealing approach to avoid restrictions in the error distribution associated with least squares fitting. We used AIC to compare models and account for a variable number of parameters.

Applying the QuickBird biomass equations (Table 1e–f) to the crown diameter (d_{crown}, m) of each tree delineated from the QuickBird data, we calculated b_{tree}, for every tree. We determined the sum of the number of trees and the sum of tree biomass for each 25 m and, separately, each 31.8 m pixel, and calculated tree density (N, trees ha^{-1}) and $B_{\text{live trees}}$ of each pixel. We estimated the standard error of $B_{\text{live trees}}$ of each pixel ($SE_{\text{field + QuickBird}}$, Mg ha^{-1}) by applying the QuickBird biomass equations (Table 1e–f) to the standard errors of crown delineation and adding the standard error of the QuickBird biomass equations that were derived from field data:

$$SE_{\text{field + QuickBird}} = N \left[\left(\frac{1 \text{ Mg}}{10^6 \text{ g}} \right) \text{Exp} \left(\alpha (SE_{\text{detect}} + SE_{\text{valid}})^\beta \right) + SE_{\text{allometric}} \right] \qquad (17)$$

where Exp(x) denotes e^x, α β, and $SE_{\text{allometric}}$ are the allometric coefficients, exponents, and standard errors (Mg), respectively, from the QuickBird biomass equations (Table 1g–i), SE_{detect} is the standard error of crown delineation (m) determined by sensitivity analysis of NDVI forest mask values and transect termination thresholds, and $SE_{\text{validation}}$ is the standard error of crown delineation (m) determined by validation of QuickBird crown estimates against field measurements. The $SE_{\text{allometric}}$ term integrates the effect of field errors into the
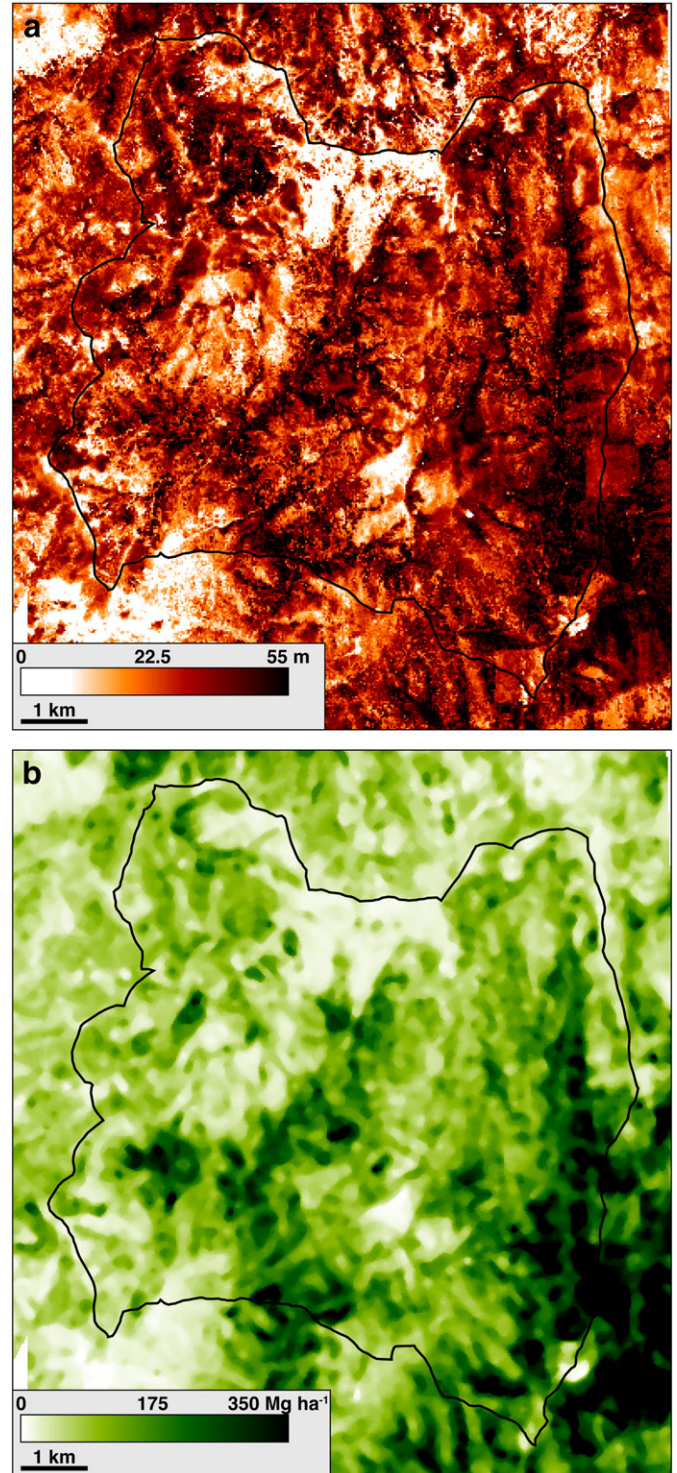

Fig. 6. North Yuba research area. (a) Lidar maximum canopy height. (b) Aboveground live tree carbon, from field measurements, Lidar, and Monte Carlo analyses.

Table 4
Aboveground forest carbon densities (Mg ha^{-1}) from field measurements, with standard errors of the mean calculated without Monte Carlo. Litter was not measured in Garcia–Mailliard.

Research area	Forest type	Live trees		Shrubs		Dead trees		Coarse woody debris		Litter		Total		n
		Mean	SE	Mean	SE	Mean	SE	Mean	SE	Mean	SE	Mean	SE	
Garcia	Secondary redwood	100	6.1	0.3	0.1	3	3.3	3	0.7	–	–	100	7.5	28
Mailliard	Old-growth redwood	310	32	0	0	8.3	2.3	2.6	1.0	–	–	320	35	12
North Yuba	Oak and Douglas-fir	210	36	0.5	0.3	10	5.9	1.3	1.2	37	7.7	260	51	6
North Yuba	Mid-elevation mixed conifer	190	3.4	1.1	0.2	19	4.7	2.0	0.6	49	5.4	260	14	30
North Yuba	Red fir	360	80	0	0	58	16	8.5	3.2	81	24	510	120	3

Table 5
Spatial autocorrelation of mean biomass density (Moran's I; Anselin, 1995).

	I_{global}				Maximum I_{local}			
	Lidar		QuickBird		Lidar		QuickBird	
	25 m	31.8 m	25 m	31.8 m	25 m	31.8 m	25 m	31.8 m
Garcia–Mailliard	0.94	0.92	0.29	0.40	0.058	0.058	0.057	0.061
North Yuba	0.99	0.98	0.37	0.50	0.004	0.004	0.001	0.001

QuickBird uncertainty estimates. We also calculated I_{local} for $B_{live\ trees}$ of each pixel at a lag of one pixel, and I_{global} for each research area.

For each research area and each spatial resolution, we calculated 100 realizations of $C_{live\ trees}$ of each pixel, adding to the mean value of $B_{live\ trees}$ a term for the combined field and QuickBird errors (Eq. (17)) and another term for spatial autocorrelation:

$$\hat{C}_{live\ trees}^{pixel} = f_C \left[\overline{B}_{live\ trees}^{pixel} + \left(X_{field\ +\ QuickBird} SE_{field\ +\ QuickBird} \right) \right. \tag{18}$$
$$\left. + \left(X_{autocorrelation} |I_{local}| SE_{field\ +\ QuickBird} \right) \right].$$

The Monte Carlo equations for Lidar (Eq. (15)) and QuickBird (Eq. (18)) have the same form. We calculated the mean (Eq. (16)), CI (Eq. (13)), and uncertainty (Eq. (14)) of the 100 realizations of $C_{live\ trees}$, for forest areas ($d_{crown} \geq$ detection limit of the crown delineation algorithm).

3. Results

3.1. Field measurements

Table 2 presents results from field measurements, including trees counted, species richness, tree diameters, tree densities, and shrub cover. Coast redwood was the most abundant species in Garcia, tanoak (*Lithocarpus densiflorus*) the most abundant in Mailliard, and Douglas-fir was the third most abundant overall (Appendix A). In North Yuba, white fir (*Abies concolor*) was most abundant and red fir (*Abies magnifica*), Douglas-fir, and sugar pine (*Pinus lambertiana*) were the next most abundant (Appendix A). Six plots fell in mixed oak–Douglas-fir forest (>90% of trees were oak or Douglas-fir), 30 plots fell in mid-elevation mixed conifer forest, and three plots fell in

red fir forest (>90% of trees were red fir) (Fig. 3a). Appendix A lists the species of shrubs or trees growing in shrub form that we recorded. Table 1g–i gives the allometric equations that we derived of biomass as a function of crown diameter.

3.2. Lidar

Table 3 presents results from Lidar, including ground elevation, canopy height, and forest area. The tree canopy in Mailliard was nearly twice as high, on average, as the tree canopy in Garcia (Fig. 5). In North Yuba, the tallest trees occurred in the lower elevations of the Empire Creek watershed in the east part of the area and in high-elevation red fir forest in the west part of the area (Fig. 6). Table 1e–f gives the regression equations derived for biomass as a function of Lidar height metrics. The form of the North Yuba equation is a height variable refined by measures of the vertical distribution of the canopy. The bimodal distribution of canopy heights in the Garcia–Mailliard data rendered percentile heights less accurate indicators of biomass than quadratic mean height. For the assessment of Lidar accuracy, linear regression of h_L of each central annular plot in Garcia–Mailliard against Lidar canopy height metrics showed significant correlation ($r = 0.94$, $P < 0.0001$, $n = 40$). In North Yuba, stepwise multiple regression of h_L of each central annular plot against Lidar canopy height metrics showed significant correlation ($R = 0.89$, $P < 0.0001$, $n = 39$).

3.3. QuickBird

Table 3 presents results from QuickBird, including number of trees delineated, tree densities, crown diameters, and forest area. Crowns in Mailliard were, on average, wider than crowns in Garcia (Fig. 2b). In North Yuba, wider crowns occurred in the mixed oak–Douglas-fir forests of the southeast part of the area (Fig. 3b). Higher tree densities occurred on southern aspects. Sensitivity analyses of NDVI forest mask values and transect termination thresholds on the 1 km^2 test areas showed an SE of 0.71 m per crown (Garcia–Mailliard) and 0.66 m per crown (North Yuba). Validation of QuickBird crown diameters against field measurements showed significant correlation (Garcia–Mailliard $r = 0.82$, $P < 0.05$, SE = 1.1 m, $n = 74$; North Yuba $r = 0.82$, $P < 0.05$, SE = 0.52 m, $n = 26$).

Table 6
Aboveground live tree carbon densities and uncertainties from Monte Carlo analyses of field measurements and remote sensing data at spatial resolutions of 25 m and 31.8 m.

Research area	Forest type	Field measurements				Lidar (25 m)			
		Mean (Mg ha^{-1})	95% CI (Mg ha^{-1})	Uncertainty (%)	n (plots)	Mean (Mg ha^{-1})	95% CI (Mg ha^{-1})	Uncertainty (%)	n (pixels)
Garcia	Secondary redwood	97	27	27	28	80	0.7	0.8	88,643
Mailliard	Old-growth redwood	310	130	42	12	200	4.1	2	1606
Garcia–Mailliard	All	100	24	24	40	82	0.6	0.8	90,249
North Yuba	All	200	90	44	39	140	0.8	0.6	66,606

3.4. Carbon density from field data

Table 4 gives carbon density for each aboveground carbon pool. In Garcia–Mailliard, carbon density was greater in old-growth coast redwood than secondary coast redwood by a factor of three. In both research areas, shrubs and coarse woody debris contained only small fractions of $C_{aboveground}$. In North Yuba, the fraction of $C_{aboveground}$ in live trees varied inversely with elevation, the opposite of the observed increase with elevation of the fraction of $C_{aboveground}$ in dead trees. Litter in North Yuba contained one-fifth of $C_{aboveground}$. Appendix A gives the fraction of $C_{live trees}$ in each area, by species.

3.5. Carbon densities from Monte Carlo analyses

Table 5 gives the spatial autocorrelation indices used in the Monte Carlo analyses. Table 6 gives aboveground live tree carbon densities and uncertainties from the field measurement, Lidar, and QuickBird Monte Carlo analyses. Uncertainties for Lidar were <1% for the two research areas, lower than for QuickBird and field measurements. Forest carbon density was substantially higher in the old-growth stands of Mailliard than the recovering secondary stands of Garcia (Fig. 5b). The highest forest carbon densities in North Yuba occurred in the taller stands in the southeast parts of the area and in some high-elevation red fir stands (Fig. 6b). Carbon density estimates did not differ appreciably between the 25 m and 31.8 m analyses. Uncertainty estimates at 31.8 m spatial resolution were slightly higher (~0.1%) than uncertainty estimates at 25 m for the two research areas.

$C_{live trees}$ for Garcia with Monte Carlo error propagation (Table 6) differed slightly from the simple mean $C_{live trees}$ values (Table 4) due to the random sampling of the Monte Carlo approach. As expected, fits and uncertainties of the Lidar-derived estimates of $B_{live trees}$ became worse when we propagated field data uncertainty through the Lidar biomass equations (Table 1e–f). For Garcia–Mailliard (Table 1e), R^2 decreased from 0.86 for the original equation to 0.83 for the median of the 1000 realizations (range 0.70–0.92). The RMSE increased from 98 Mg ha^{-1} for the original equation to a median of 184 Mg ha^{-1} for all 1000 realizations (range 95–364 Mg ha^{-1}). For North Yuba (Table 1f), R^2 for both the original equation and the median of the 1000 realizations was 0.80, but R^2 for individual iterations ranged from 0.66 to 0.91. RMSE increased from 123 Mg ha^{-1} for the original equation to a median of 205 Mg ha^{-1} for all 1000 realizations (range 123–437 Mg ha^{-1}).

4. Discussion

4.1. Uncertainty estimates

Large sample sizes (>40,000 pixels) in the Monte Carlo analyses of both remote sensing systems generated low estimates of uncertainty. Lidar produced slightly lower uncertainties than QuickBird, consistent with a different comparison of Lidar and QuickBird (Hyde et al., 2006). When calibrated by field measurements and analyzed with a Monte Carlo approach, Lidar can provide forest carbon estimates with uncertainties lower than most other existing remote sensing systems, which generally produce uncertainties up to 15% (Lu, 2006). Lidar

uncertainties were lower than the 4% to 22% uncertainties of FIA forest carbon estimates for California forests (Christensen et al., 2008). Nevertheless, only field measurements made possible the calibration and validation of the remote sensing data and the quantification of the 3–30% of total aboveground biomass in shrubs, dead trees, coarse woody debris, and litter.

Spatial autocorrelation of biomass was high at the level of the research area (I_{global}). This was expected because high-biomass areas are more likely to be located near other high-biomass areas. In contrast, low values of the index of spatial autocorrelation of biomass at the pixel level (I_{local}) produced low estimates of the component of uncertainty from spatial autocorrelation.

In general, the spatial resolution of remote sensing analyses should not be finer than the size of the field plots used to calibrate the remote sensing (Næsset, 2002). The small magnitude of the differences between our 25 m and 31.8 m analyses (Table 6) suggests that results can be similar over a small range of spatial resolutions, as previously demonstrated (Zhao et al., 2009).

Calculation of forest carbon densities at the level of the research area produced considerably lower estimates of uncertainty than estimates calculated pixel-by-pixel. Mean uncertainties at the level of the pixel were high (Lidar Garcia–Mailliard 24%, North Yuba 18%; QuickBird Garcia–Mailliard 44%, North Yuba 21%) and showed little difference between 25 m and 31.8 m spatial resolutions. While the 100 carbon density realizations for each pixel varied considerably, pixel-level variations tended to cancel each other out when summarized across the entire research area. Higher uncertainties at the level of the research area in Mailliard, compared to the larger Garcia area, demonstrate this effect of large sample sizes on uncertainty. This suggests that the method that we use is more appropriate to analyses of large sample sizes, although the relatively small 1 km^2 Mailliard Redwoods SNR provided a sample size sufficient to produce an estimate of uncertainty of 3%.

4.2. Lidar and QuickBird

The close correlation of biomass to height in Northern California forests kept Lidar uncertainty low. Regression of field-measured height in North Yuba against calculated aboveground biomass (Appendix A) showed high correlation ($r = 0.99$, $n = 362$ trees). As previously demonstrated (Patenaude et al., 2004), Lidar shows an enhanced capability to estimate carbon densities in heterogeneous forests where field measurements alone may not be adequate. In our research areas, Lidar consistently produced estimates of $C_{live trees}$ lower than field estimates, suggesting that Lidar captured a more complete sample of areas of low tree density than the field sample, where we relocated plots that had randomly fallen in non-forest areas. Application of the Lidar biomass regression equations to Northern California forests with species composition and canopy structure similar to the Garcia–Mailliard and North Yuba forests is possible.

The financial expenses of renting an airplane and a Lidar sensor system and the labor time and technical expertise required for analysis may render Lidar infeasible for many users. The cost of Lidar would need to fall before it could be deployed at a large scale, e.g. in national REDD

QuickBird (25 m)				Lidar (31.8 m)				QuickBird (31.8 m)			
Mean (Mg ha^{-1})	95% CI (Mg ha^{-1})	Uncertainty (%)	n (pixels)	Mean (Mg ha^{-1})	95% CI (Mg ha^{-1})	Uncertainty (%)	n (pixels)	Mean (Mg ha^{-1})	95% CI (Mg ha^{-1})	Uncertainty (%)	n (pixels)
70	1.2	2	90,164	80	0.7	0.9	54,776	68	1.5	2	56,572
180	8.5	5	1478	200	7.1	3	982	170	9.5	5	949
71	1.2	2	91 642	82	0.7	0.9	55,758	70	1.5	2	57,521
140	1.0	0.7	80,880	140	0.9	0.6	41,224	140	1.1	0.8	52,019

programs. NASA ICESat is the only satellite currently in operation with a Lidar sensor, although its spatial resolution of 170 m is coarse for many forestry applications (Boudreau et al., 2008). A satellite Lidar sensor of finer spatial resolution would still require extensive field measurements of trees for validation and calibration. A higher density of Lidar shots per unit area would remove one constraint of our Lidar data, whose sparse density precluded identification of tree tops and validation against individual tree measurements.

The application of Lidar technology to topographic mapping and forestry applications has become widespread. In industrialized countries, the number of private companies that offer airplane, Lidar, and data analysis services has grown, ameliorating practical considerations for projects at sub-national scales. Lidar has also been used for forest carbon estimation in the Brazilian Amazon (Asner, 2009). Still, Lidar cannot sense through clouds, so the cloud cover of tropical forest areas remains a constraint.

QuickBird produced estimates of forest carbon density that were lower and estimates of uncertainty that were higher than Lidar for each research area. One source of the difference was the use of stand-level metrics from Lidar, in contrast to individual tree dimensions from QuickBird. Delineation of individual trees (QuickBird) proved more difficult to accomplish than estimation of stand-level heights (Lidar). QuickBird estimates of tree density were one-half (Garcia–Mailliard) to one-quarter (North Yuba) of the densities of trees of $dbh \geq 19.5$ cm in the field plots. This suggests a systematic undercount of trees and underestimation of carbon density, despite uncertainties

of carbon density estimates as low as 1%. QuickBird forest carbon estimates were precise, but inaccurate.

The problems with QuickBird data arose from the great height and high density of the trees in Northern California forests. These conditions produced shadows up to 25 m long that often obscured any regular patterns of bright crown tops and dark crown perimeters. The conditions also created some anomalous areas of brightness at locations other than crown tops. The shadows and anomalous bright areas hindered the ability of the automated crown detection algorithm to accurately locate crown tops, trace crown perimeters, or locate trees with relatively smaller crowns (Fig. 7). Pixel-by-pixel differences between the carbon density estimates from QuickBird and Lidar, as a fraction of Lidar carbon density, did not vary substantially with slope. This suggests that topography itself is not the main factor leading to differences between Lidar and QuickBird, although topography can contribute to forming the shadows and anomalous bright areas that challenged the automated crown detection algorithm.

Previous attempts at crown delineation from high-resolution optical satellites mitigated inter-crown shadow problems through the completely manual tracing of tree crowns by people (Asner et al., 2002; Clark et al., 2004). Whereas manual crown delineation may be possible for research on areas ≤ 0.5 km^2 with hundreds of trees, labor and time requirements rendered manual interpretation infeasible for our operational tests on areas >50 km^2 with hundreds of thousands of trees. In addition, a person may not be able to reliably assess the small changes in pixel brightness associated with the precise edge of a tree
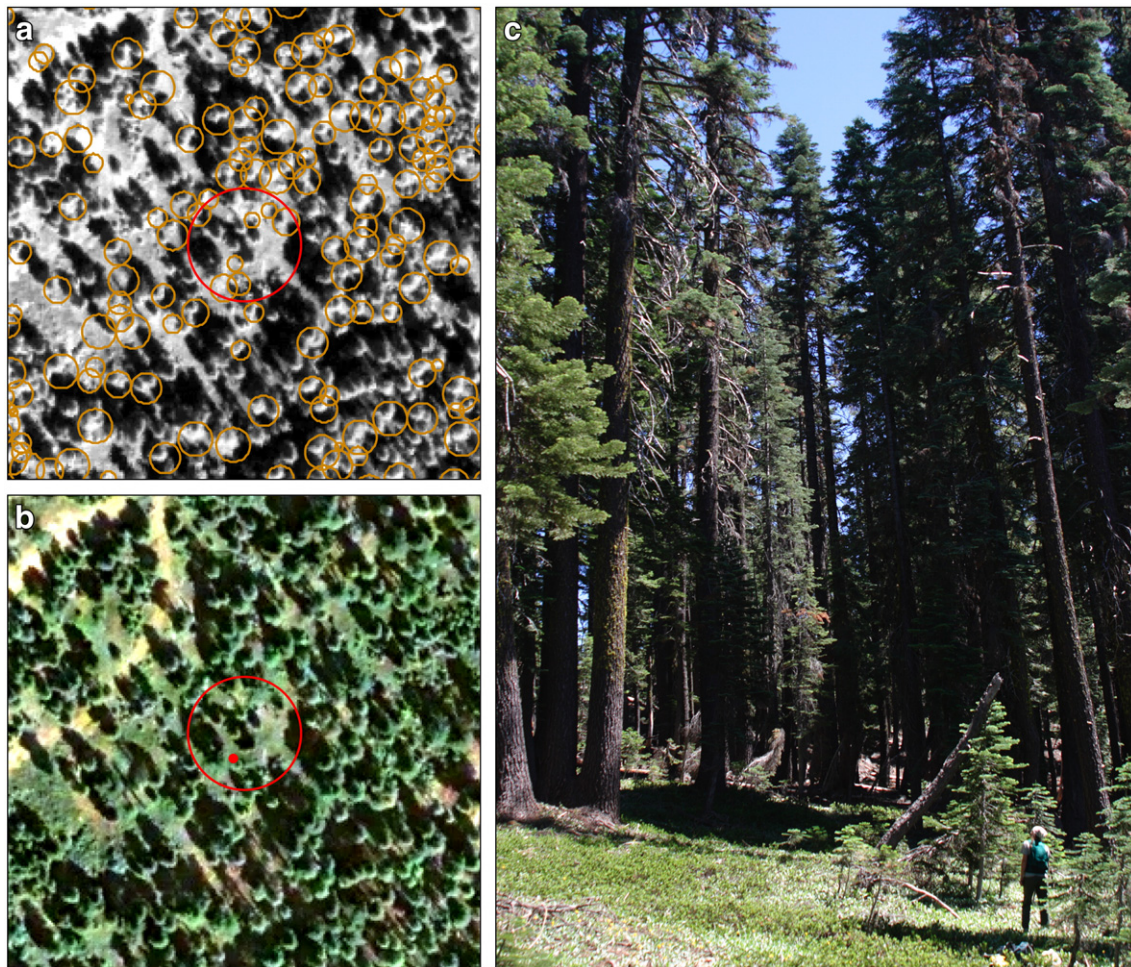

Fig. 7. QuickBird satellite image at North Yuba plot B4. (a) Panchromatic image, 150 m × 150 m, 0.6 m spatial resolution. The red circle is the 17.95 m radius central annular field plot. Orange circles are tree crowns delineated by the automated detection algorithm, which omitted numerous trees in the area. (b) Panchromatic-sharpened multi-spectral image, 0.6 m spatial resolution. (c) Photograph taken approximately from the red dot in (b) and looking northeast, 10 days before acquisition of the QuickBird image. The dominant tree species is red fir (*Abies magnifica*).

crown. Maintaining consistency of interpretation among different people could prove challenging. Despite the intensive attention represented by manual interpretation, merging of small tree crowns in images and missed detection of understory trees can introduce significant inaccuracies (Asner et al., 2002).

Automated crown detection approaches decrease the labor and time requirements of image analysis and can increase analytical accuracy (Culvenor, 2002; Gougeon, 1995; Lowell, 1998; Palace et al., 2008). Our test, however, confirms previously observed problems with inter-crown shadows in high-resolution satellite images (Asner & Warner, 2003; Wulder et al., 2004) and with missed detection of understory trees (Broadbent et al., 2008). Moreover, accuracy of automated methods varies with sensor and solar angle (Wulder et al., 2004). Consequently, automated methods require image-by-image customization, further increasing processing time. In our tests, a ratio of crown diameter to image spatial resolution of approximately 15:1 (9 m crown/0.6 m image) or higher provided adequate crown detection, but numerous trees of smaller crown diameter remained undetected. Satellite acquisition at times of high solar angle could partially mitigate inter-crown shadow problems. Despite the crown detection difficulties, acquisition of data from QuickBird and other high-resolution satellites remains logistically simpler than Lidar data acquisition.

In addition to providing robust estimates of forest carbon density, the methods that we tested, combining field measurements, remote sensing, and Monte Carlo analysis, produced wall-to-wall spatial data layers of forest carbon. Wall-to-wall spatial data derived from remote sensing can show planners of forest carbon projects the spatial distribution of carbon and facilitate the targeting of forest conservation actions.

4.3. Forest carbon densities

Field measurements revealed that red fir forest contains the highest densities of carbon and the lowest densities of trees in North Yuba. This reflects the high proportion of old-growth trees in red fir forest, in contrast to mixed oak and Douglas-fir forest, which had the highest tree densities and lowest carbon densities.

We found carbon densities in old-growth coast redwood forest, old-growth Sierra Nevada red fir, and old-growth Sierra Nevada mixed conifer (Table 4) that substantially exceed the average forest carbon densities of FIA plots in these California forest types (Christensen et al., 2008) and are at the high end of the range for old-growth stands in these California forest types (Hudiburg et al., 2009). Aboveground carbon densities of old-growth coast redwood forest and Sierra Nevada forest (Table 4) equal or exceed the aboveground carbon densities of 100–190 Mg ha^{-1} in Amazon rainforest (Baker et al., 2004) and Congo rainforest (Zhang & Justice, 2001) and average aboveground carbon densities of all major forest types around the world (Aalde et al., 2006). Based on Lidar results, we estimate (mean ± CI) that Garcia–Mailliard contains 450,000 ± 3800 t of carbon and North Yuba contains 590,000 ± 3300 t of carbon. Together these forests store an amount of carbon equivalent to the annual greenhouse gas emissions (U.S. Department of Energy, 2008) of a U.S. city of approximately 160,000 people.

5. Conclusions

Using Lidar, QuickBird, and field measurements, we have shown that:

1. Airborne Lidar provides forest carbon estimates with lower uncertainty and higher accuracy than QuickBird high-resolution satellite data.
2. Monte Carlo analyses of uncertainties from field measurements, remote sensing accuracy, regression equations, and spatial auto-correlation can reduce the uncertainty of forest carbon density

estimates to levels lower than published forest inventory carbon estimates.
3. A method that combines field measurements, Lidar, and Monte Carlo analysis can produce wall-to-wall spatial data layers and robust estimates of forest carbon.
4. Sierra Nevada and coast redwood forests in California contain carbon at densities as high or higher than tropical rainforest.

Appendix A. Supplementary data

Supplementary data associated with this article can be found, in the online version, at doi: 10.1016/j.rse.2010.02.011.

References

Aalde, H., Gonzalez, P., Gytarsky, M., Krug, T., Kurz, W. A., Ogle, S., et al. (2006). Forest land. Intergovernmental Panel on Climate Change, *National Greenhouse Gas Inventory Guidelines*, vol. 4. (pp. 4.1−4.83)Hayama, Japan: Institute for Global Environmental Strategies.

Achard, F., Eva, H. D., Mayaux, P., Stibig, H. J., & Belward, A. (2004). Improved estimates of net carbon emissions from land cover change in the tropics for the 1990s. *Global Biogeochemical Cycles*, 18, GB2008. doi:10.1029/2003GB002142

Andersen, H. E., Reutebuch, S. E., & McGaughey, R. J. (2006). A rigorous assessment of tree height measurements obtained using airborne lidar and conventional field methods. *Canadian Journal of Remote Sensing*, 32, 355−366.

Anselin, L. (1995). Local indicators of spatial association−LISA. *Geographical Analysis*, 27, 93−115.

Asner, G. P., & Warner, A. S. (2003). Canopy shadow in the LBA IKONOS satellite archive: Implications for multispectral studies of tropical forests and savannas. *Remote Sensing of Environment*, 87, 521−533.

Asner, G. P., Palace, M., Keller, M., Pereira, R., Silva, J. N. M., & Zweede, J. C. (2002). Estimating canopy structure in an Amazon forest from laser range finder and IKONOS satellite observations. *Biotropica*, 34, 483−492.

Asner, G. P. (2009). Tropical forest carbon assessment: Integrating satellite and airborne mapping approaches. *Environmental Research Letters*, 4, 034009. doi: 10.1088/1748-9326/4/3/034009

Baker, T. R., Phillips, O. L., Malhi, Y., Almeida, S., Arroyo, L., Di Fiore, A., et al. (2004). Increasing biomass in Amazonian forest plots. *Philosophical Transactions of the Royal Society of London B*, 359, 353−365.

Balzter, H., Rowland, C. S., & Saich, P. (2007). Forest canopy height and carbon estimation at Monks Wood National Nature Reserve, UK, using dual-wavelength SAR interferometry. *Remote Sensing of Environment*, 108, 224−239.

Barrett, D. J., Galbally, I. E., & Graetz, R. D. (2001). Quantifying uncertainty in estimates of C emissions from above-ground biomass due to historic land-use change to cropping in Australia. *Global Change Biology*, 7, 883−902.

Bartholomé, E., & Belward, A. S. (2005). GLC2000: A new approach to global land cover mapping from Earth observation data. *International Journal of Remote Sensing*, 26, 1959−1977.

Bickel, K., Richards, G., Köhl, M., & Rodrigues, R. L. V. (2006). Consistent representation of lands. Intergovernmental Panel on Climate Change, *National Greenhouse Gas Inventory Guidelines*, vol. 4. (pp. 3.1−3.42)Hayama, Japan: Institute for Global Environmental Strategies.

Blackard, J. A., Finco, M. V., Helmer, E. H., Holden, G. R., Hoppus, M. L., Jacobs, D. M., et al. (2008). Mapping U.S. forest biomass using nationwide forest inventory data and moderate resolution information. *Remote Sensing of Environment*, 112, 1658−1677.

Boudreau, J., Nelson, R. F., Margolis, H. A., Beaudoin, A., Guindon, L., & Kimes, D. S. (2008). Regional aboveground forest biomass using airborne and spaceborne LiDAR in Quebec. *Remote Sensing of Environment*, 112, 3876−3890.

Broadbent, E. N., Asner, G. P., Pena-Claros, M., Palace, M., & Soriano, M. (2008). Spatial partitioning of biomass and diversity in a lowland Bolivian forest: Linking field and remote sensing measurements. *Forest Ecology and Management*, 255, 2602−2616.

Brown, J. K. (1974). Handbook for inventorying down woody material. *General technical report INT-16*. Ogden, UT: U.S. Department of Agriculture, Forest Service.

Burnham, K. P., & Anderson, D. R. (1998). *Model selection and multimodel inference: A practical information-theoretic approach.* New York: Springer-Verlag.

Busing, R. T., & Fujimori, T. (2005). Biomass, production and woody detritus in an old coast redwood (*Sequoia sempervirens*) forest. *Plant Ecology, 177*, 177–188.

California Department of Forestry and Fire Protection. (2003). Land Cover Mapping and Monitoring Program, Vegetation Data. http://frap.cdf.ca.gov

Canham, C. D., & Uriarte, M. (2006). Analysis of neighborhood dynamics of forest ecosystems using likelihood methods and modeling. *Ecological Applications, 16*, 62–73.

Chambers, J. Q., Fisher, J. I., Zeng, H., Chapman, E. L., Baker, D. B., & Hurtt, G. C. (2007). Hurricane Katrina's carbon footprint on U.S. Gulf Coast forests. *Science, 318*, 1107.

Christensen, G. A., Campbell, S. J., & Fried, J. S. (Eds.). (2008). California's forest resources, 2001–2005: Five-year forest inventory and analysis report. *General technical report PNW-GTR-763.* Portland, OR: U.S. Department of Agriculture, Forest Service.

Clark, D. B., Read, J. M., Clark, M., Cruz, A. M., Dotti, M. F., & Clark, D. A. (2004). Application of 1-m and 4-m resolution satellite data to studies of tree demography, stand structure and land use classification in tropical rain forest landscapes. *Ecological Applications, 14*, 61–67.

Culvenor, D. S. (2002). TIDA: An algorithm for the delineation of tree crowns in high spatial resolution imagery. *Computers and Geosciences, 28*, 33–44.

DeFries, R., Achard, F., Brown, S., Herold, M., Murdiyarso, D., Schlamadinger, B., et al. (2007). Earth observations for estimating greenhouse gas emissions from deforestation in developing countries. *Environmental Science and Policy, 10*, 385–394.

Drake, J. B., Dubayah, R. O., Clark, D. B., Knox, R. G., Blair, J. B., Hofton, M. A., et al. (2002). Estimation of tropical forest structural characteristics using large-footprint LIDAR. *Remote Sensing of Environment, 79*, 305–319.

Edwards, A. W. F. (1992). *Likelihood.* Baltimore, MD: John Hopkins University Press.

Fahey, T. J., Woodbury, P. B., Battles, J. J., Goodale, C. L., Hamburg, S., Ollinger, S., et al. (2009). Forest carbon storage: Ecology, management, and policy. *Frontiers in Ecology and the Environment.* doi:10.1890/080169

Gougeon, F. A. (1995). A crown following approach to the automatic delineation of individual tree crowns in high spatial resolution digital images. *Canadian Journal of Remote Sensing, 26*, 274–284.

Hanus, M. L., Marshall, D. D., & Hann, D. W. (1999). Height–diameter equations for six species in the coastal regions of the Pacific Northwest. *Forest Research Laboratory research contribution, 25.* Corvallis, OR: Oregon State University.

Harmon, M.E., & Sexton, J. (1996). Guidelines for measurements of woody detritus in forest ecosystems. Long Term Ecological Research Network, http://intranet.lternet.edu/archives/documents/Publications/woodydetritus

Hudiburg, T., Law, B., Turner, D. P., Campbell, J., Donato, D., & Duane, M. (2009). Carbon dynamics of Oregon and Northern California forests and potential land-based carbon storage. *Ecological Applications, 19*, 163–180.

Hurtt, G. C., Dubayah, R., Drake, J., Moorcroft, P. R., Pacala, S. W., Blair, J. B., et al. (2004). Beyond potential vegetation: Combining lidar data and a height-structured model for carbon studies. *Ecological Applications, 14*, 873–883.

Husch, B., Beers, T. W., & Kershaw, J. A. (2003). *Forest mensuration*, 4th Edition. Hoboken, NJ: John Wiley & Sons.

Hyde, P., Dubayah, R., Walker, W., Blair, J. B., Hofton, M., & Hunsaker, C. (2006). Mapping forest structure for wildlife habitat analysis using multi-sensor (LiDAR, SAR/InSAR, ETM+, Quickbird) synergy. *Remote Sensing of Environment, 102*, 63–73.

Intergovernmental Panel on Climate Change. (2006). *National greenhouse gas inventory guidelines.* Hayama, Japan: Institute for Global Environmental Strategies.

Intergovernmental Panel on Climate Change. (2007). *Climate change 2007: The physical science basis.* Cambridge, UK: Cambridge University Press.

Jenkins, J. C., Chojnacky, D. C., Heath, L. S., & Birdsey, R. A. (2003). National-scale biomass estimators for United States tree species. *Forest Science, 49*, 12–35.

Jenkins, J. C., Chojnacky, D. C., Heath, L. S., & Birdsey, R. A. (2004). Comprehensive database of diameter-based biomass regressions for North American tree species. *General technical report NE-319.* Newtown Square, PA: U.S. Department of Agriculture, Forest Service.

Larsen, D. R., & Hann, D. W. (1987). Height-diameter equations for seventeen tree species in Southwest Oregon. *Forest Research Laboratory research paper, 49.* Corvallis, OR: Oregon State University.

Le Quéré, C., Raupach, M. R., Canadell, J. G., Marland, G., Bopp, L., Ciais, P., et al. (2009). Trends in the sources and sinks of carbon dioxide. *Nature Geoscience, 2*, 831–836.

Lefsky, M. A., Cohen, W. B., Acker, S. A., Spies, T. A., Parker, G. G., & Harding, D. (1999). Lidar remote sensing of biophysical properties and canopy structure of forest of Douglas-fir and western hemlock. *Remote Sensing of Environment, 70*, 339–361.

Lefsky, M. A., Cohen, W. B., & Spies, T. A. (2001). An evaluation of alternate remote sensing products for forest inventory, monitoring, and mapping of Douglas-fir forests in western Oregon. *Canadian Journal of Forest Research, 31*, 78–87.

Lefsky, M. A., Hudak, A. T., Cohen, W. B., & Ackerd, S. A. (2005). Geographic variability in lidar predictions of forest stand structure in the Pacific Northwest. *Remote Sensing of Environment, 95*, 532–548.

Loveland, T. R., Reed, B. C., Brown, J. F., Ohlen, D. O., Zhu, Z., Yang, L., et al. (2000). Development of a global land cover characteristics database and IGBP DISCover from 1-km AVHRR data. *International Journal of Remote Sensing, 21*, 1303–1330.

Lowell, K. (1998). Evaluation of a moving-window algorithm for detecting individual tree stems from scanned aerial photographs in Victoria's eucalyptus forests. *Australian Forestry, 61*, 226–234.

Lu, D. (2006). The potential and challenge of remote sensing-based biomass estimation. *International Journal of Remote Sensing, 27*, 1297–1328.

Magnussen, S., & Boudewyn, P. (1998). Derivations of stand heights from airborne laser scanner data with canopy-based quantile estimators. *Canadian Journal of Forest Research, 28*, 1016–1031.

Mandel, J. (1984). *The statistical analysis of experimental data.* Mineola, NY: Dover Publications.

Matthews, E., Payne, R., Rohweder, M., & Murray, S. (2000). *Pilot analysis of global ecosystems: Forest ecosystems.* Washington, DC: World Resources Institute.

McGroddy, M. E., Daufresne, T., & Hedin, L. O. (2004). Scaling of C:N:P stoichiometry in forests worldwide: Implications of terrestrial Redfield-type ratios. *Ecology, 85*, 2390–2401.

Means, J. (2005). Forest Science Data Bank: TP072, Pacific Northwest Plant Biomass Component Equation Library. H.J. Andrews Experimental Forest, Long Term Ecological Research Site, http://andrewsforest.oregonstate.edu/data/abstract.cfm?dbcode=TP072

Monni, S., Peltoniemi, M., Palosuo, T., Lehtonen, A., Mäkipää, R., & Savolainen, I. (2007). Uncertainty of forest carbon stock changes—Implications to the total uncertainty of GHG inventory of Finland. *Climatic Change, 81*, 391–413.

Næsset, E. (1997). Determination of mean tree height of forest stands using airborne laser scanner data. *ISPRS Journal of Photogrammetry and Remote Sensing, 52*, 49–56.

Næsset, E. (2002). Predicting forest stand characteristics with airborne scanning laser using a practical two-stage procedure and field data. *Remote Sensing of Environment, 80*, 88–99.

Næsset, E. (2009). Effects of different sensors, flying altitudes, and pulse repetition frequencies on forest canopy metrics and biophysical stand properties derived from small-footprint airborne laser data. *Remote Sensing of Environment, 113*, 148–159.

Næsset, E., & Gobakken, T. (2008). Estimation of above- and below-ground biomass across regions of the boreal forest zone using airborne laser. *Remote Sensing of Environment, 112*, 3079–3090.

Olson, J. S., Watts, J. A., & Allison, L. J. (1983). *Carbon in live vegetation of major world ecosystems.* Oak Ridge, TN: U.S. Department of Energy.

Palace, M., Keller, M., Asner, G. P., Hagen, S., & Braswell, B. (2008). Amazon forest structure from IKONOS satellite data and the automated characterization of forest canopy properties. *Biotropica, 40*, 141–150.

Patenaude, G., Hill, R. A., Milne, R., Gaveau, D. L. A., Briggs, B. B. J., & Dawson, T. P. (2004). Quantifying forest above ground carbon content using LiDAR remote sensing. *Remote Sensing of Environment, 93*, 368–380.

Pillsbury, N. H., & Kirkley, M. L. (1984). Equations for total, wood, and saw-log volume for thirteen California hardwoods. *Research note PNW-414.* Portland, OR: U.S. Department of Agriculture, Forest Service.

Potter, C., Gross, P., Klooster, S., Fladeland, M., & Genovese, V. (2008). Storage of carbon in U.S. forests predicted from satellite data, ecosystem modeling, and inventory summaries. *Climatic Change, 90*, 269–282.

Saatchi, S. S., Houghton, R. A., dos Santos Alvalá, R. C., Soares, J. V., & Yu, Y. (2007). Distribution of aboveground live biomass in the Amazon basin. *Global Change Biology, 13*, 816–837.

Sánchez-Azofeifa, G. A., Castro-Esau, K. L., Kurz, W. A., & Joyce, A. (2009). Monitoring carbon stocks in the tropics and the remote sensing operational limitations: From local to regional projects. *Ecological Applications, 19*, 480–494.

Sexton, J. O., Bax, T., Siqueira, P., Swenson, J. J., & Hensley, S. (2009). A comparison of lidar, radar, and field measurements of canopy height in pine and hardwood forests of southeastern North America. *Forest Ecology and Management, 257*, 1136–1147.

Ter-Mikaelian, M. T., & Korzukhin, M. D. (1997). Biomass equations for sixty-five North American tree species. *Forest Ecology and Management, 97*, 1–24.

Thenkabail, P. S., Enclona, E. A., Ashton, M. S., Legg, C., & De Dieu, M. J. (2004). Hyperion, IKONOS, ALI, and ETM+ sensors in the study of African rainforests. *Remote Sensing of Environment, 90*, 23–43.

Tucker, C. J. (1979). Red and photographic infrared linear combinations for monitoring vegetation. *Remote Sensing of Environment, 8*, 127–150.

United States Department of Agriculture, Forest Service. (2004a). *Forest inventory and analysis national core field guide, volume I: Field Data collection procedures for phase 2 plots.* Washington, DC: U.S. Department of Agriculture, Forest Service.

United States Department of Agriculture, Forest Service. (2004b). *Sierra Nevada forest plan amendment, final supplemental environmental impact statement, record of decision.* Vallejo, CA: U.S. Department of Agriculture, Forest Service.

United States Department of Agriculture, Forest Service. (2009). Forest Inventory Data Online. http://fiatools.fs.fed.us/fido/index.html

United States Department of Energy. (2008). Emissions of greenhouse gases in the United States 2007. *Report DOE/EIA-0573(2007).* Washington, DC: U.S. Department of Energy.

van Mantgem, P. J., & Stephenson, N. L. (2005). The accuracy of matrix population model projections for coniferous trees in the Sierra Nevada, California. *Journal of Ecology, 93*, 737–747.

von Storch, H., & Zwiers, F. W. (1999). *Statistical analysis in climate research.* Cambridge, UK: Cambridge University Press.

Wang, G., Gertner, G. Z., Fang, S., & Anderson, A. B. (2005). A methodology for spatial uncertainty analysis of remote sensing and GIS products. *Photogrammetric Engineering and Remote Sensing, 71*, 1423–1432.

Wensel, L. C., & Krumland, B. E. (1983). Volume and taper relationships for redwood, Douglas-fir, and other conifers in California's North Coast. *Division of Agricultural Science bulletin 1907.* Berkeley, CA: University of California.

Westman, W. E. (1987). Aboveground biomass, surface area, and production relations of red fir (*Abies magnifica*) and white fir (*A. concolor*). *Canadian Journal of Forest Research, 17*, 311–319.

Woodbury, P. B., Smith, J. E., & Heath, L. S. (2007). Carbon sequestration in the U.S. forest sector from 1990 to 2010. *Forest Ecology and Management, 241*, 14–27.

Woolley, T. J., Harmon, M. E., & O'Connell, K. B. (2007). Estimating annual bole biomass production using uncertainty analysis. *Forest Ecology and Management, 253*, 202–210.

Wulder, M. A., White, J. C., Niemann, K. O., & Nelson, T. (2004). Comparison of airborne and satellite high spatial resolution data for the identification of individual trees with local maxima filtering. *International Journal of Remote Sensing*, *25*, 2225−2232.

Zhang, K., Chen, S. C., Whitman, D., Shyu, M. L., Yan, J., & Zhang, C. (2003). A progressive morphological filter for removing nonground measurements from airborne LIDAR data. *IEEE Transactions on Geoscience and Remote Sensing*, *41*, 872−882.

Zhang, Q., & Justice, C. O. (2001). Carbon emissions and sequestration potential of central African ecosystems. *Ambio*, *30*, 351−355.

Zhao, K., Popescu, S., & Nelson, R. (2009). Lidar remote sensing of forest biomass: A scale-invariant estimation approach using airborne lasers. *Remote Sensing of Environment*, *113*, 182−196.

Gonzalez, P., G.P. Asner, J.J. Battles, M.A. Lefsky, K.M. Waring, and M. Palace. 2010. Forest carbon densities and uncertainties from Lidar, QuickBird, and field measurements in California. *Remote Sensing of Environment* 114: 1561-1575.

Appendix A.

Table 1. Height equations, for comparison of Lidar height metrics to field-estimated Lorey's mean height.

Research area	Species	Equation	r^2	n
North Yuba	*Abies concolor*	$h = (225.815\ dbh)/(424.225 + dbh)$	0.87	140
North Yuba	*Abies magnifica*	$h = -0.0958 + 0.4380\ dbh$	0.63	65
North Yuba	*Calocedrus decurrens*	$h = (50.55\ dbh)/(78.40 + dbh)$	0.69	15
North Yuba	hardwood species	$h = (84.88\ dbh)/(136.13 + dbh)$	0.28	62
North Yuba	*Pinus lambertiana*	$h = (140.26\ dbh)/(241.19 + dbh)$	0.82	68
North Yuba	*Pinus monticola*	$h = (71.52\ dbh)/(159.77 + dbh)$	0.87	7
North Yuba	*Pinus jeffreyi* and *Pinus ponderosa*	$h = 0.0646 + 0.4256\ dbh$	0.50	16
North Yuba	*Pseudotsuga menziesii*	$h = (91.33\ dbh)/(108.95 + dbh)$	0.84	39
Garcia	*Lithocarpus densiflorus*	$h = (37.17\ dbh)/(35.69 + dbh)$	0.46	63
Garcia	*Pseudotsuga menziesii*	$h = (54.99\ dbh)/(38.33 + dbh)$	0.70	71
Garcia	*Quercus chrysolepis*	$h = (23.37\ dbh)/(19.86 + dbh)$	0.31	20
Garcia	*Sequoia sempervirens*	$h = (46.06\ dbh)/(45.37 + dbh)$	0.56	67
Garcia	other species	$h = (28.53\ dbh)/(17.82 + dbh)$	0.33	41
Mailliard	*Lithocarpus densiflorus*	$h = (192.52\ dbh)/(265.73 + dbh)$	0.64	27
Mailliard	*Pseudotsuga menziesii*	$h = (104.50\ dbh)/(96.06 + dbh)$	0.91	11
Mailliard	*Sequoia sempervirens*	$h = (97.49\ dbh)/(108.77 + dbh)$	0.80	37
Mailliard	other species	$h = (47.61\ dbh)/(45.23 + dbh)$	0.49	27

Variables: dbh = diameter at breast height (cm, at height = 1.37 m), h = height (m), n = number of trees in sample, r^2 = coefficient of determination.

Table 2. Allometric equations, to calculate biomass from field measurements. Wood density from Jenkins et al. (2004) was used to convert from volume to biomass, except for *Sequoia sempervirens*.

Species	Equation	Units (b, v, dbh, h)	Source
Abies concolor	$\ln(b_{tree}) = 4.36982 + 2.5043 \ln(dbh)$	g, _, cm, _	Westman 1987
Abies concolor	$\ln(b_{stem\,no\,bark}) = 3.11845 + 2.7011 \ln(dbh)$	g, _, cm, _	Westman 1987
Abies concolor	$\ln(b_{bark}) = 2.36182 + 2.6201 \ln(dbh)$	g, _, cm, _	Westman 1987
Abies magnifica	$\ln(b_{tree}) = 2.61856 + 2.9121 \ln(dbh)$	g, _, cm, _	Westman 1987
Abies magnifica	$\ln(b_{stem\,no\,bark}) = 2.55249 + 2.7821 \ln(dbh)$	g, _, cm, _	Westman 1987
Abies magnifica	$\ln(b_{bark}) = 1.46053 + 2.8468 \ln(dbh)$	g, _, cm, _	Westman 1987
Acer macrophyllum	$\ln(b_{bark}) = 2.3338 + 2.574 \ln(dbh)$	g, _, cm, _	Means 2005
Acer macrophyllum	$\ln(b_{stem\,no\,bark}) = 3.4148 + 2.723 \ln(dbh)$	g, _, cm, _	Means 2005
Acer macrophyllum	$\ln(b_{foliage}) = 3.14276 + 1.617 \ln(dbh)$	g, _, cm, _	Means 2005
Acer macrophyllum	$\ln(b_{live\,branches}) = 2.67176 + 2.430 \ln(dbh)$	g, _, cm, _	Means 2005
Acer macrophyllum	$\ln(b_{dead\,branches}) = 4.7918 + 1.092 \ln(dbh)$	g, _, cm, _	Means 2005
Arbutus menziesii	$v_{tree} = 0.0000821921\ dbh^{1.96628}h^{0.83458}$	_, m³, cm, m	Pillsbury and Kirkley 1984
Arbutus menziesii	$v_{tree} = 0.0000378129\ dbh^{1.99295}h^{1.01532}$	_, m³, cm, m	Pillsbury and Kirkley 1984
Calocedrus decurrens	$\ln(b_{stem}) = 2.112422 + 2.7818 \ln(dbh)$	g, _, cm, _	Means 2005
Cornus nuttallii	$b_{tree} = \mathrm{Exp}(-2.48 + 2.4835 \ln(dbh))$	kg, _, cm, _	Jenkins et al. 2003
Lithocarpus densiflorus	$\ln(v_{tree}) = 0.3484045 + 1.94165 \ln(dbh) + 0.86562 \ln(h)$	_, cm³, cm, cm	Means 2005
Lithocarpus densiflorus	$\ln(v_{stem\,no\,bark}) = -3.150511 + 2.19576 \ln(dbh) + 1.14078 \ln(h)$	_, cm³, cm, cm	Means 2005
Pinus jeffreyi	$\ln(b_{stem}) = 1.817891 + 2.952 \ln(dbh)$	g, _, cm, _	Means 2005
Pinus lambertiana	$\ln(b_{stem\,no\,bark}) = -3.984 + 2.6667 \ln(dbh)$	kg, _, cm, _	Jenkins et al. 2004
Pinus lambertiana	$\ln(b_{bark}) = -5.295 + 2.6186 \ln(dbh)$	kg, _, cm, _	Jenkins et al. 2004
Pinus lambertiana	$\ln(b_{live\,branches}) = -7.637 + 3.3648 \ln(dbh)$	kg, _, cm, _	Jenkins et al. 2004
Pinus lambertiana	$\ln(b_{dead\,branches}) = -5.413 + 2.172 \ln(dbh)$	kg, _, cm, _	Jenkins et al. 2004
Pinus lambertiana	$\ln(b_{foliage}) = -4.023 + 2.0327 \ln(dbh)$	kg, _, cm, _	Jenkins et al. 2004
Pinus lambertiana	$\ln(b_{new\,foliage}) = -5.846 + 2.085 \ln(dbh)$	kg, _, cm, _	Jenkins et al. 2004

Species	Equation	Units (b, v, dbh, h)	Source
Pinus monticola	$b_{tree} = 20800 + 0.1544\ dbh^2h$	g, _, cm, cm	Means 2005
Pinus monticola	$b_{bark} = 1200 + 0.0112\ dbh^2h$	g, _, cm, cm	Means 2005
Pinus monticola	$b_{stem\ no\ bark} = 2300 + 0.1204\ dbh^2h$	g, _, cm, cm	Means 2005
Pinus ponderosa	$b_{stem\ no\ bark} = 0.011\ dbh^{2.7587}$	kg, _, cm, _	Ter-Mikaelian and Korzukhin 1997
Pinus ponderosa	$b_{bark} = 0.0144\ dbh^{2.2312}$	kg, _, cm, _	Ter-Mikaelian and Korzukhin 1997
Pinus ponderosa	$b_{foliage} = 0.0119\ dbh^{2.0967}$	kg, _, cm, _	Ter-Mikaelian and Korzukhin 1997
Pinus ponderosa	$b_{live\ branches} = 0.0045\ dbh^{2.7185}$	kg, _, cm, _	Ter-Mikaelian and Korzukhin 1997
Pseudotsuga menziesii (coast)	$\ln(b_{foliage}) = 4.0616 + 1.7009\ \ln(dbh)$	g, _, cm, _	Means 2005
Pseudotsuga menziesii (coast)	$\ln(b_{live\ branches}) = 3.2137 + 2.1382\ \ln(dbh)$	g, _, cm, _	Means 2005
Pseudotsuga menziesii (coast)	$\ln(b_{dead\ branches}) = 3.3788 + 1.7503\ \ln(dbh)$	g, _, cm, _	Means 2005
Pseudotsuga menziesii (coast)	$\ln(b_{stem\ no\ bark}) = 3.8682 + 2.5951\ \ln(dbh)$	g, _, cm, _	Means 2005
Pseudotsuga menziesii (coast)	$\ln(b_{bark}) = 2.5975 + 2.43\ \ln(dbh)$	g, _, cm, _	Means 2005
Pseudotsuga menziesii (Sierra)	$b_{tree} = 1054 + 0.2057\ dbh^2h$	g, _, cm, cm	Means 2005
Pseudotsuga menziesii (Sierra)	$b_{stem} = -115 + 0.1896\ dbh^2h$	g, _, cm, cm	Means 2005
Quercus agrifolia	$b_{tree} = \text{Exp}(-2.0127 + 2.4342\ \ln(dbh)$	kg, _, cm, _	Jenkins et al. 2003
Quercus chrysolepsis	$\ln(v_{tree}) = 1.4735389 + 2.20527\ \ln(dbh) + 0.6119\ \ln(h)$	_, cm³, cm, cm	Means 2005
Quercus chrysolepsis	$\ln(v_{stem\ no\ bark}) = -0.211699 + 2.32519\ \ln(dbh) + 0.74348\ \ln(h)$	_, cm³, cm, cm	Means 2005
Quercus kelloggii	$\ln(v_{tree}) = 0.5509162 + 1.97437\ \ln(dbh) + 0.85034\ \ln(h)$	_, cm³, cm, cm	Means 2005
Quercus kelloggii	$\ln(v_{stem\ no\ bark}) = -0.183607 + 2.12635\ \ln(dbh) + 0.83339\ \ln(h)$	_, cm³, cm, cm	Means 2005
Sequoia sempervirens (old-growth)	$\log_{10}(v_{stem\ no\ bark}) = 0.9784\ \log_{10}(dbh^2h) - 0.4843$	_, m³, m, m	Busing and Fujimori 2005
Sequoia sempervirens (secondary)	$v_{stem\ no\ bark} = 0.0283 * 0.0007903 * (3.28\ dbh)^{1.792}\ (3.28\ h)^{1.282}$	_, m³, m, m	Wensel and Krumland 1983

Species	Equation	Units (b, v, dbh, h)	Source
Sequoia sempervirens (old-growth)	$b_{tree} = 0.38 \; 1.12 \; v_{stem\,no\,bark}$	t, m^3, _, _	Busing and Fujimori 2005
Sequoia sempervirens (secondary)	$b_{tree} = 0.33 \; 1.12 \; v_{stem\,no\,bark}$	t, m^3, _, _	Busing and Fujimori 2005
Torreya californica	$b_{tree} = \mathrm{Exp}(-2.5384 + 2.4814 \ln(dbh))$	kg, _, cm, _	Jenkins et al. 2003
Umbellaria californica	$b_{tree} = \mathrm{Exp}(-2.48 + 2.4835 \ln(dbh))$	kg, _, cm, _	Jenkins et al. 2003

Variables: b_{bark} = biomass of bark of stem, $b_{dead\,branches}$ = biomass of dead branches, $b_{foliage}$ = foliage biomass, $b_{live\,branches}$ = biomass of live branches, $b_{new\,foliage}$ = biomass of new foliage, b_{stem} = biomass of stem with bark, $b_{stem\,no\,bark}$ = biomass of stem without bark, b_{tree} = total aboveground biomass of a tree, dbh = diameter at breast height (at height = 1.37 m), $\mathrm{Exp}(x) = e^x$, h = height, $v_{stem\,no\,bark}$ = volume of stem without bark, v_{tree} = total aboveground tree volume.

Table 3. Fraction (%) of trees and forest carbon (C) in each area, by species, for trees of *dbh* ≥ 19.5 cm.

Species	Common name	North Yuba		Garcia		Mailliard	
		trees	C	trees	C	trees	C
Abies concolor	white fir	46	50				
Abies magnifica	red fir	14	20				
Acer macrophyllum	bigleaf maple	1	<1			1	<1
Arbutus menziesii	Pacific madrone			5	6	6	3
Calocedrus decurrens	incense cedar	3	1				
Lithocarpus decurrens	tanoak			27	47	50	22
Pinus jeffreyi	jeffrey pine	<1	<1				
Pinus lambertiana	sugar pine	9	9	3	2		
Pinus monticola	western white pine	1	1				
Pinus ponderosa	ponderosa pine	1	2				
Pseudotsuga menziesii	Douglas-fir	10	13	28	29	16	38
Quercus agrifolia	coast live oak			1	1		
Quercus chrysolepis	canyon live oak	6	1	3	2	1	<1
Quercus kelloggii	California black oak	9	3	2	2		
Sequoia sempervirens	coast redwood			28	9	24	36
Torreya californica	California nutmeg			1	<1	2	<1
Umbellularia californica	California laurel			1	2	<1	<1

Table 4. Species of shrubs or trees growing in shrub form recorded in the field plots.

Species	Common name	Garcia-Mailliard	North Yuba
Acer glabrum	mountain maple		√
Arctostaphylos nevadensis	pinemat manzanita		√
Arctostaphylos patula	greenleaf manzanita		√
Chrysolepis sempervirens	bush chinquapin		√
Cornus nuttallii	Pacific dogwood		√
Quercus chrysolepis	canyon live oak		√
Quercus vaccinifolia	huckleberry oak		√
Quercus wislizeni	interior live oak	√	
Rubus sp.	blackberry		√
Symphoricarpos mollis	creeping snowberry		√
Vaccinium caespitosum	dwarf huckleberry		√
Vaccinium ovatum	evergreen huckleberry	√	